INFLUENCE OF UV LIGHT AND HEAT ON THE FERROELECTRIC PROPERTIES OF LITHIUM NIOBATE CRYSTALS

Dissertation
zur
Erlangung des Doktorgrades (Dr. rer. nat.)
der
Mathematisch-Naturwissenschaftlichen Fakultät
der
Rheinischen Friedrich-Wilhelms-Universität Bonn

vorgelegt von
Hendrik Steigerwald

aus
Neuwied am Rhein

Bonn 2011

Angefertigt mit Genehmigung der Mathematisch-Naturwissenschaftlichen Fakultät der Rheinischen Friedrich-Wilhelms-Universität Bonn

1. Gutachter:	Prof. Dr. Karsten Buse
2. Gutachter:	Prof. Dr. Karl Maier

Tag der Promotion: 19.5.2011
Erscheinungsjahr: 2011

Contents

Chapter 1

Introduction

> ”Allwissend bin ich nicht;
> doch viel ist mir bewusst.” [1]

Since the advent of the laser [2], optical technologies have become a part of everyday-life. Applications in fields such as life science [3], medicine [4], and material processing [5] have exploited this new light source for many yearsand even nowadays fields of application such as home media [6] still trigger the need for low-cost and mass-producible lasers. Despite the huge demand, even today the optical spectrum between the IR and the UV is not fully accessible by laser sources. The dark lines of the ”rainbow” spanned by the different laser types, e.g. in the regime of green light [7], can be filled by nonlinear optics. Optical parametric oscillation [8] and second harmonic generation [9] are two possible mechanisms to convert light to different wavelengths that both benefit from quasi phase matching [10, 11]. The two mechanisms are based on high-quality non-linear crystals.

One of the most important non-linear-optical materials is lithium niobate [12, 13], due to its ease of fabrication, robustness, transparency in the visible-to-infrared and excellent nonlinear properties [14]. Lithium niobate possesses a shift between the distribution of the cations and the anions, at room temperature, along the crystalographic *c*-axis, leading to a so-called spontaneous polarization. Although, it was once considered to be a ”frozen ferroelectric” [15], during the last couple of decades the possibility to influence the orientation of the spontaneous polarization of lithium niobate and therefore its ferroelectricity has become a vivid field of research [16, 17]. The possibility to tailor ferroelectric domains allows for a wealth of applications [18, 19] and therefore it is of special interest. But many of the applications of lithium niobate involve high light intensities. Since the material is photorefractive, at high light intensities the beam profile is distorted, which is then called optical damage [20]. Doping of lithium niobate with magnesium suppresses the undesirable optical damage [21], making it usable for high-power applications, but it also leads to some new challenges in terms of domain structuring.

Several techniques have been developed to generate ferroelectric domain structures in lithium niobate crystals [22–24]. Currently, the most common method for ferroelectric domain patterning in bulk crystals is applying an electric field by structured electrodes located on one of the *c*-faces of the crystal [25]. The locally modulated field causes local reorienting of the spontaneous polarization. Unfortunately, this method becomes more challenging for magnesium-doped material [26] and the smallest bulk domain structures that would be desirable [18] have not been realized yet.

In this thesis the issue of tailoring ferroelectric domain structures is approached from two sides: interaction of defect structures inside the crystal with growing ferroelectric domains is investigated and also actual domain patterning on all crystal faces by different methods is performed. Special emphasis is given to the Mg-doped material. The fundamental understanding and the methods of domain patterning developed in this thesis are then used to obtain tailored domain structures that meet the requirements of their intended application in non-linear optics.

Chapter 2

Fundamentals

The versatile, tunable features of lithium niobate enable various optical applications. In this chapter the general properties of lithium niobate are reviewed first and then the ferroelectric properties of this material, which lie within the scope of this thesis, are summarized.

2.1 Lithium niobate crystals – general properties

2.1.1 Crystal structure and symmetry

Lithium niobate ($LiNbO_3$) is a birefringent, piezo- and pyroelectric crystal that exists in its ferroelectric phase below the Curie temperature of $T_C = 1411\,\mathrm{K}$ [13]. The crystal structure, which belongs to the point group $3m$ [12], is invariant under a 120°rotation and exhibits a mirror plane containing the rotation axis, the *c*-axis of the crystal. In this work the *z*-axis of the cartesian coordinate system is parallel to the *c*-axis. The orientation of the *c*-axis is given by the position of the two cations lithium (Li) and niobium (Nb) as well as the vacancies (□) with respect to the oxygen planes, where the $+c$ direction is defined by the sequence: ..., Li, Nb, □, Li, Nb, □, ... (Fig. 2.1). The displacement of the cations relative to the center between two oxygen planes along the polar *c*-axis gives rise to the dipoles leading to the spontaneous polarization [27]:

$$P_S = 0.71\,\mathrm{C/m^2}\ . \tag{2.1}$$

When $LiNbO_3$ crystals are heated up to T_C, which lies below the melting temperature of 1520 K [13], the displacement and therefore the spontaneous polarization vanishes. A second-order phase transition from ferroelectric to paraelectric takes place [28].

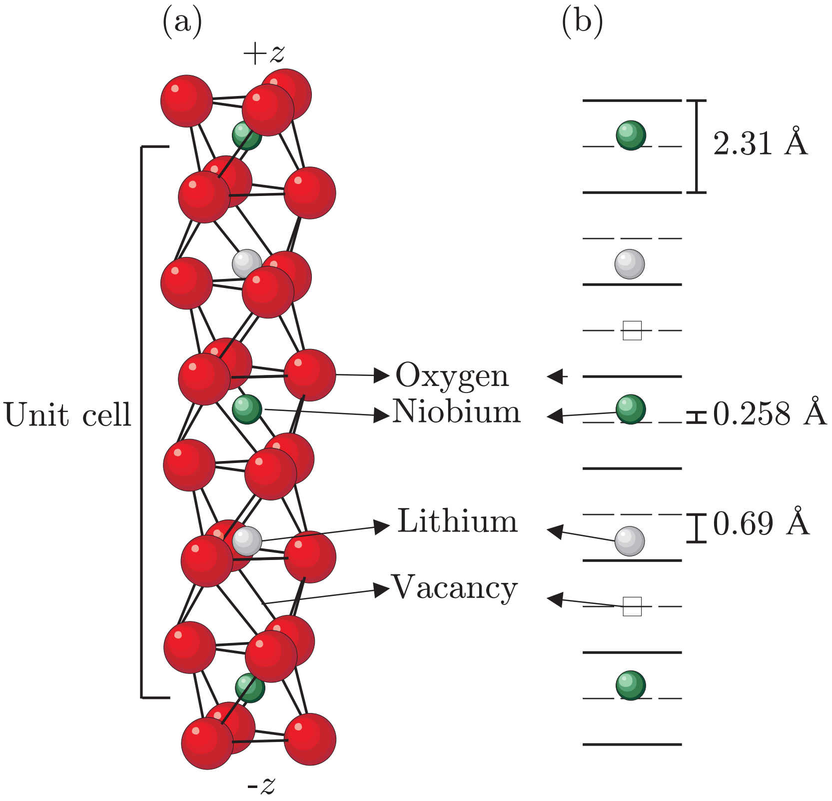

Figure 2.1: (a) The crystal structure of $LiNbO_3$ replotted from [29]. (b) The relative positions of the cations (Li, Nb) in relation to the oxygen planes represented by black lines. The dashed lines represent the center plane between two oxygen planes.

2.1.2 Characteristic absorption

The transparency range of undoped, congruently melting $LiNbO_3$ (CLN) extends from a wavelength around 4.5 µm down to the UV edge around 350 nm, where the photon energy exceeds the band gap of the crystal (3.7 eV) [13]. Beyond this absorption edge, the exact position of which depends on stoichiometry and doping [30], light absorption increases strongly, so that below 300 nm the absorption length is on the order of a few microns [31–33]. A prominent absorption peak, which results from small amounts of hydrogen bound to the oxygen, is called the OH-peak and can be found at $\lambda = 2.87$ µm [34]. An important feature of the absorption properties is that they can be utilized to determine the stoichiometry [35] and the degree of doping with magnesium, e.g. by the shift of the OH-peak which indicates a doping level that is sufficient to suppress the optical damage [36].

2.1.3 Stoichiometry, defects and doping

The standard method for the fabrication of $LiNbO_3$ is to grow the crystal by the Czochralski method. This method leads to a congruently melting composition of the crystal. The melt consists only of 48.5 % Li_2O, which ensures a uniform composition of the boule throughout the fabrication process. This Li deficiency [36], incorporated into the crystal structure, causes intrinsic defect structures, based on Nb-ions, sitting on Li-sites that are charge-compensated by four Li-vacancies. A possible structure for this the so-called Nb_{Li}-antisite defect cluster was proposed by Kim et al. for undoped congruent $LiNbO_3$ (see Fig. 2.2) [29, 37, 38]. For the case of Mg-doped congruent $LiNbO_3$, where the magnesium atoms replace the Nb-ions sitting on the Li-sites [39], the structure of the defect cluster has yet to be determined. These antisite defect clusters possess a dipole moment, which can be aligned either parallel or antiparallel with regard to the spontaneous polarization.

Crystals that have an atomic Li:Nb-ratio of 1:1 are called stoichiometric $LiNbO_3$ (SLN). They can be obtained either by growing them directly from the melt by the double crucible Czochralski method [40] or by performing vapor transport equilibration on non-stoichiometric $LiNbO_3$ [41].

One drawback of congruently melting $LiNbO_3$ is that its applicability in non-linear optics is hampered by optical damage [20]. This manifests in beam distortion at high laser intensities, caused by the bulk photovoltaic effect, which leads to a local change of the refractive index via the electro-optic effect [42, 43]. An increase of the photoconductivity, e.g. by

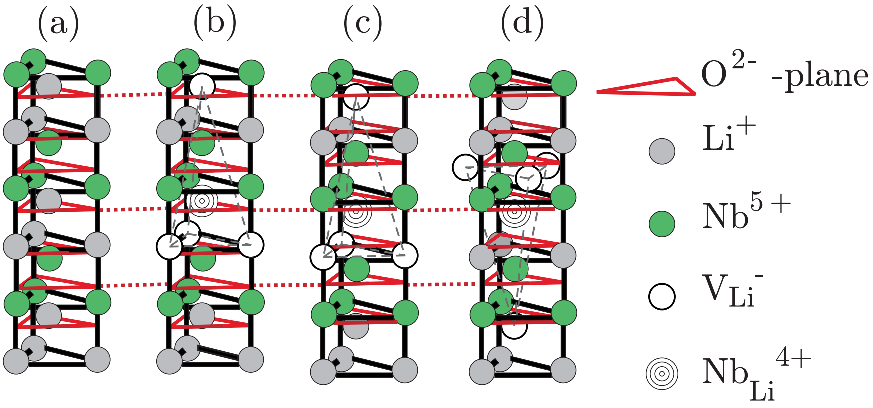

Figure 2.2: Schematics of a defect complex proposed by Kim et al. involving a niobium-on-lithium antisite defect (Nb_{Li}) and lithium vacancies (V_{Li}) in CLN [29, 38]. A stoichiometric crystal without defects is shown in (a). The defect complex depicted in (b), after domain inversion, becomes a frustrated defect with antiparallel orientation of its dipole moment with regard to the *c*-axis (c). At elevated temperatures the lithium vacancies redistribute and the dipole complex aligns itself parallel to the *c*-axis again (d).

doping the crystal with more than 5 mol% magnesium or usage of SLN, suppresses optical damage significantly [21].

2.2 Lithium niobate as a ferroelectric material

The ferroelectric properties of $LiNbO_3$ have been subject to extensive research, since $LiNbO_3$ with structured ferroelectric domains is utilized for second harmonic generation via quasi-phase matching [44, 45]. The basic concept of domain patterning and ways how to visualize ferroelectric domains are reviewed in the following.

2.2.1 Domain inversion

The term "ferroelectric" actually refers to materials with a spontaneous polarization P_S with two or more orientational states, which can be altered by application of an external electric field [28]. In the case of $LiNbO_3$, the spontaneous polarization has two possible orientations, namely parallel or antiparallel to the initial orientation of the crystal *c*-axis [28]. Application of an electrical field of sufficient magnitude reorients P_S [25, 46]. During the domain inversion process, the Li- and Nb-ions shift their position along the *c*-axis, where the Li-ions move into the next oxygen octahedron, whereas the Nb-ions only move to the opposite side of the symmetry plane inside their oxygen octahedron. The shift of the cations yields an inversion of the crystallographic *c*-axis (see Fig. 2.3).

The plane between two domains is called a domain wall. Due to the change of the sign of the spontaneous polarization P_S, the compensation charge on the *z*-faces have to be redistributed, which yields the following equation for the amount of redistributed charge (Q) depending on the domain-inverted area A:

$$Q = 2P_S A \, . \tag{2.2}$$

The poling current I depends on the domain wall velocity. Therefore we can write

$$I(t) = 2P_S \frac{dA}{dt} \, , \tag{2.3}$$

where dA/dt is the change of the domain inverted area on the *z*-face per time. The poling behavior of $LiNbO_3$ is reflected in the temporal evolution of I, namely discontinuous domain wall motion that leads to poling current peaks, the so-called Barkhausen jumps [47].

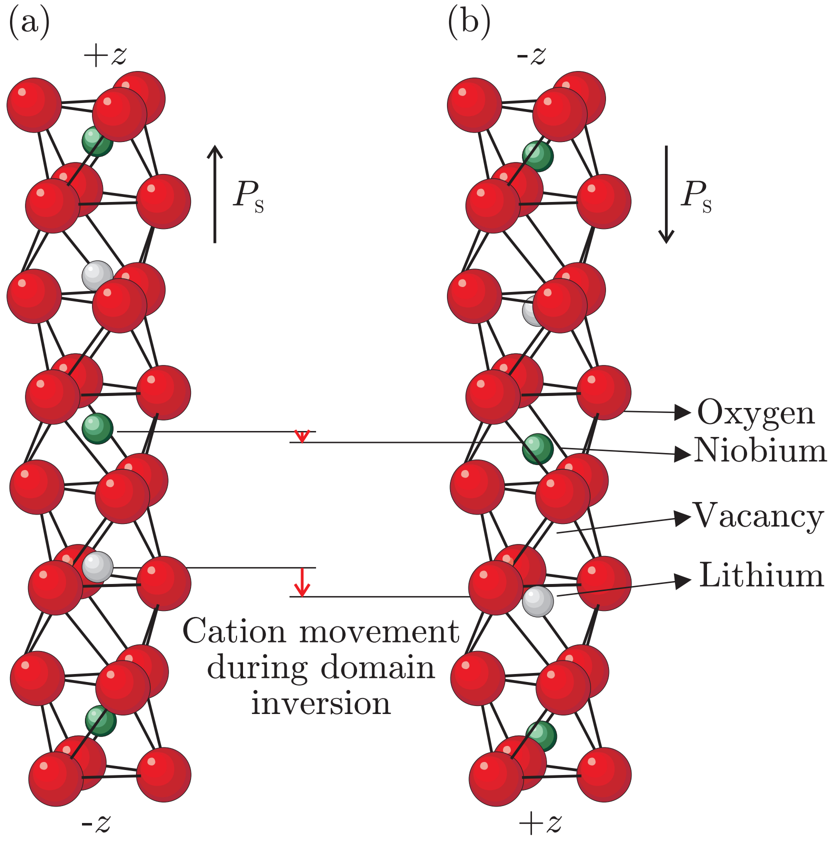

Figure 2.3: Schematics of a $LiNbO_3$ unit cell (a) before and (b) after domain inversion. Movement of the cations relative to the oxygen planes yields an inversion of the spontaneous polarization P_S.

During domain inversion, due to reasons of symmetry, all crystal properties represented by tensors with rank 1, 3 or 5 change their sign. In particular this applies to the non-linear susceptibility, so periodic modulation of P_S yields periodic modulation of the non-linear susceptibility, which is the basic concept of quasi-phase matching [48].

The most common definition for coercive field (E_C) is the threshold electric field that has to be applied to invert P_S from its initial orientation, and for $LiNbO_3$ it scales between 21 kV/mm and 2 kV/mm, depending on the stoichiometry [49–52] and the doping [53, 54] of the crystal.

For two subsequent domain inversions of $LiNbO_3$, the spontaneous polarization can be plotted vs. the applied external field, showing a hysteresis loop (see Fig. 2.4). The magnitude of the forward and backward switching field can be read from the intersection of the loop with the E-axis and in this thesis E_C is defined as the value of the forward switching field [55]. For congruent material the value of the backward switching field that reorients P_S is smaller than E_C. This is probably caused by an internal field, generated by the antisite defect clusters (see Fig. 2.2) [38, 49, 55], which do not necessarily flip their polarization.

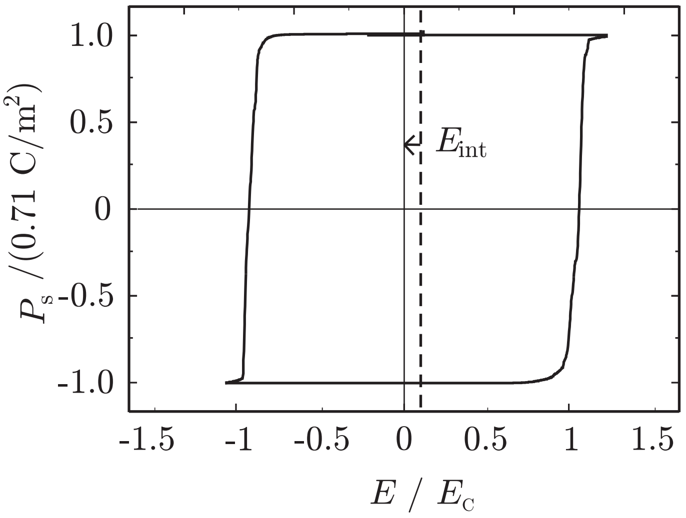

Figure 2.4: Spontaneous polarization P_S of $LiNbO_3$ plotted vs. the applied electrical field E normalized to the coercive fiueld E_C. The shift of the hysteresis loop due to the so-called internal field (E_{int}) is indicated by the dashed line.

2.2.2 Coercive field reduction

There are various intrinsic and extrinsic parameters that affect the coercive field of $LiNbO_3$. In terms of intrinsic parameters, the coercive field depends on the stoichiometry, since defects have a major influence on the domain inversion process. The Nb_{Li} antisite defect can pin domain walls [37, 56], therefore the composition of the $LiNbO_3$ crystal has a significant effect on E_C. Doping of the crystal with cations that replace the Nb-ion sitting on the Li-site [57], e.g., Mg-, Mn- or Er-ions, reduces E_C [58–60]. Since converging the Li-to-Nb ratio to 1:1 inside the crystal yields reduction of the domain wall pinning, crystals with a composition closer to that of SLN have a lower coercive field [49–52].

There is also extrinsic treatment that can reduce the coercive field. Illumination with visible light [61, 62] or weakly absorbed UV light [63] decreases E_C transiently. In the case of weakly absorbed UV light, significant E_C reduction is only observed in crystals with Mg-doping above the threshold that suppresses the optical damage [54].

Heating of the crystal to 500 K during EFP transiently reduces the coercive field of $LiNbO_3$ to less than 50% of its value at room temperature [37, 64]. The internal field is reduced, so that the required field for forward poling and the field for backward poling converge to the same value for increasing temperature. Fewer Barkhausen jumps are observed at elevated temperatures, indicating smoother domain wall propagation (see Eq. 2.3) [37].

2.2.3 Domain patterning

There are several techniques available for domain patterning. Yamada et al. were the first to demonstrate periodic poling of $LiNbO_3$ at room temperature by using an electron beam [65]. Nowadays, the most common technique is electric field poling (EFP), which can be performed using structured metal electrodes [25] or liquid electrodes with a structured dielectric resist on the crystal surface [66]. When applying a voltage to the electrodes that produces an external field which exceeds the coercive field, the domains nucleate at the edges of the electrodes, where the field is the highest [67]. The domains start growing along the z-axis, while they simultaneously spread perpendicular to the z-axis. Due to different aspects of domain kinetics [68] it is challenging to generate domain patterns with period lengths of a few microns in bulk crystals, especially for magnesium-doped $LiNbO_3$ [26]. It is still an active field of research to develop new methods for domain structuring that yield smaller ratios for domain width to domain depth in periodically poled material. Light-assisted domain patterning by spatial modulation of E_C utilizing structured illumination by weakly absorbed UV light has been performed to realize bulk domain patterns with shorter period lengths in MgCLN [63, 69]. For 500-µm-thick MgCLN crystals bulk domain patterns with a period length of 16 µm have been generated. Periodic domain patterning is performed at elevated temperature from 350 K to 440 K to obtain a better aspect ratio of the domain width to the depth of the domain pattern [70, 71].

Domain patterning also can be obtained directly during the crystal growth process [17, 44], by titanium in-diffusion [72], electron bombardment [73], exposure to focussed visible light [61], scanning electron beams [65] or ion beams [74]. Another method, which allows for domain patterning in the nm-regime is poling by application of a voltage to the tip of a scanning force microscope [75, 76]. The possibilities and underlying mechanisms of domain engineering by strongly absorbed UV light [24, 77, 78] and EFP assisted by weakly absorbed UV light [54, 63] are exploited in the context of this thesis.

2.2.4 Domain visualization

Several methods for domain visualization have been introduced which have various benefits and disadvantages [79, 80]. The domain visualization methods used in this thesis are described in the following.

At the vicinity of domain walls in $LiNbO_3$, strong mechanical strain-induced birefringence is observed due to the photoelastic effect [12]. This effect can be utilized to visualize domain walls in z-cut crystals through crossed polarizers [81], which offers the possibility of non-destructive in-situ visualization [82].

Another method to visualize domains, which works only on the y- and z-faces of $LiNbO_3$, is domain selective etching [83–86], where the fact that the $-z$ and $-y$ faces can be etched, whereas the $+z$ and $+y$ faces remain almost unaffected, translates a domain pattern into the corresponding topography pattern. This is then imaged by optical microscopy, or with even higher spatial resolution by scanning electron microscopy or atomic force microscopy. Aqueous hydrofluoric acid (HF) [19] or mixtures based on HF [87] are commonly used for domain-selective etching. The etching rate for the $-z$ face of $LiNbO_3$ is 0.8 µm/h [86] and for the $-y$ face it is $0.08 - 0.11$ µm/h [88] at room temperature. Despite the advantage of high spatial resolution, HF-etching is a destructive method that limits the usefulness of the domain-engineered crystal for further application.

Recently, piezoresponse force microscopy (PFM) has become an alternate method for domain visualization, based on a modified scanning force microscope [80, 89]. An oscillating voltage is applied to the PFM-tip, while the crystal is scanned in contact mode. The PFM domain signal is detected by a lock-in amplifier, measuring the tip cantilever vibration and its phase with respect to that of the applied modulated voltage, caused by the surface thickness change generated by the piezoelectric effect. PFM offers a lateral domain resolution in the nm-regime, is non-destructive and can detect domains on all faces of $LiNbO_3$ with a depth resolution up to 2 µm [90].

Chapter 3

Experimental methods

In this section different approaches are introduced to control domain inversion in $LiNbO_3$ and generate domain patterns. Experimental methods to investigate the effect of strongly absorbed UV light, weakly absorbed UV light and heat on the domain inversion process are described.

3.1 Samples

Lithium niobate crystals are fabricated in boules and mostly sold in the form of wafers, where CLN is typically sold as 4″ wafers and SLN or doped CLN is typically sold as 3″ wafers. The orientation of the crystallographic axes is indicated by the so-called flats, flattenings on the circular wafer, which are indicated to be perpendicular to one of the crystallographic axes. $LiNbO_3$ wafers with different compositions, which all have a thickness of 500 µm and surfaces polished to optical grade, are investigated. Whereas for the EFP experiments only samples from z-cut wafers are used, the experiments on domain generation by strongly absorbed UV light are also conducted with samples of x- and y-cut wafers. The z-cut wafers are cut into samples with dimensions of $x \times y = 15\,\text{mm} \times 16\,\text{mm}$ and the x- and y-cut wafers are cut into samples with dimensions of $y \times z = 12\,\text{mm} \times 13\,\text{mm}$ and $x \times z = 15\,\text{mm} \times 14\,\text{mm}$, respectively, to enable identification of their crystallographic axes by the shape of the sample. Table 3.1 gives an overview of all samples used, their manufacturer, their stoichiometry and their doping.

Additionally to the usage of as-grown crystals, a set of CLN z-cut crystals is annealed in vacuum (6×10^{-4} mbar) at 1070 K for 8 h. Through chemical reduction, this procedure leads to the formation of stable bipolarons with an absorption band centered at the of wavelength 500 nm [93].

Sample name	Stoichiometry	Doping level	Cut orientation
CLN	Congruent	–	z
MgCLN	Congruent	5 mol%	z
MgSLN	Near-stoichiometric	1 mol%	z
SLN	Stoichiometric	–	z
CLN(y)	Congruent	–	y
MgCLN(x)	Congruent	5 mol%	x

Table 3.1: List of all types of $LiNbO_3$ crystals used in this thesis. Manufacurers: CLN/ CLN(y): Crystal Technology Inc. (USA), MgCLN/ MgCLN(x): Yamaju Ceramics Co. Ltd (Japan), SLN/ MgSLN: Oxide Corp. (Japan). All crystals have a thickness of 500 µm. The near-stoichiometric magnesium-doped samples and the congruent magnesium-doped samples are both doped above the corresponding threshold, so that optical damage is suppressed [91, 92].

3.2 Experimental setup for domain inversion

To achieve domain inversion in $LiNbO_3$ crystals by electrical field poling (EFP), high electrical fields up to 21 kV/mm are required. Since the electrical breakdown field in air is around 3 kV/mm and currents in the regime of just several µA have to be measured to determine the coercive field, the crystal holder has to have good insulating properties. Furthermore, the impact of UV illumination and heating on the coercive field is investigated, so the poling setup has to enable simultaneous illumination with light down to a wavelength of 300 nm and controlled heating up to 520 K during EFP.

3.2.1 Sample holder

The basic concept of the sample holder is that a z-cut $LiNbO_3$ crystal is clamped between two O-rings by two fused silica plates and then is contacted from both faces by liquid electrodes. A schematic view of the sample holder is shown in Fig. 3.1. The O-rings have an inner diameter of 9 mm, so the area on each face contacted by the liquid electrodes is $0.64 - 0.71\,\mathrm{cm}^2$, depending on how strong the O-rings are clamped and therefore deformed.

At room temperature, O-rings made of graphite-free silicon are used, which at temperatures above 400 K are replaced by O-rings made of viton®, which has a higher thermal resistivity. The two fused silica plates are transparent for visible light and UV light down to 200 nm and each have two holes, drilled from the top, to fill in the liquid electrodes and hence to contact both crystal faces. The $+z$ face is connected to a high-voltage amplifier (Trek 20C), which can deliver voltages from -20 kV to $+20$ kV. The electrode on the $-z$ face is used to determine the poling current, which is on the order of several µA. The electrode is either connected to an amperemeter (Keithley 6514 Electrometer) for the case of slow poling by voltage ramps or to a current-to-voltage converter connected in series to an oscilloscope (Agilent 54624A) to detect the poling current for the case of poling with short high voltage pulses.

At room temperature, the conductivity of the CLN, MgCLN, SLN, and MgSLN samples is below $10^{-12}\,\Omega^{-1}\mathrm{m}^{-1}$ and corresponds to the so-called dark conductivity of the crystal σ_{D}. Therefore, the resulting background current of a 500-µm-thick sample at 10 kV is below 1 nA and negligible in comparison to the poling current. The overall conductivity of the samples is given by:

$$\sigma = \sigma_{\mathrm{D}} + \sigma_{\mathrm{Ph}} + \sigma_{\mathrm{I}}. \tag{3.1}$$

The ionic conductivity σ_{I} rises with increasing temperature, while the photoconductivity σ_{Ph}, in this experiment, depends on the intensity of the weakly absorbed UV light.

3.2.2 Domain patterning with structured electrodes

To generate periodic domain patterns by EFP, the crystal was coated on the $+z$ face with a 1.5-µm-thick, structured photoresist. The layer of photoresist (AZ1512) acts as an electrical insulator and also absorbs 48% of the incident UV light at the wavelength of 334 nm. The photoresist pattern had a period length of 10 µm, and the stripes of the pattern were oriented parallel to the y-axis of the crystal. When the coated crystal is contacted by liquid electrodes, the duty cycle of the resulting electrode pattern on the $+z$ face is 0.1, i.e., 90% of the crystal surface is covered by the photoresist and therefore insulated, even though a duty cycle of the resulting domains of 0.5 is desired. This is due to the fact that the photoresist patterns are designed for domain patterning in magnesium-doped $\mathrm{LiNbO_3}$, where the lateral domain growth leads to rapid domain merging, while the domains grow from the $+z$ to the $-z$ face [68]. The $-z$ face is homogeneously contacted by a liquid electrode.

Customized voltage pulses with duration of 200 ms are generated by a function generator and amplified by the Trek 20C. In-situ observation of domain growth and monitoring of the poling current are used to determine when a domain pattern with a duty cycle close to 0.5 has been

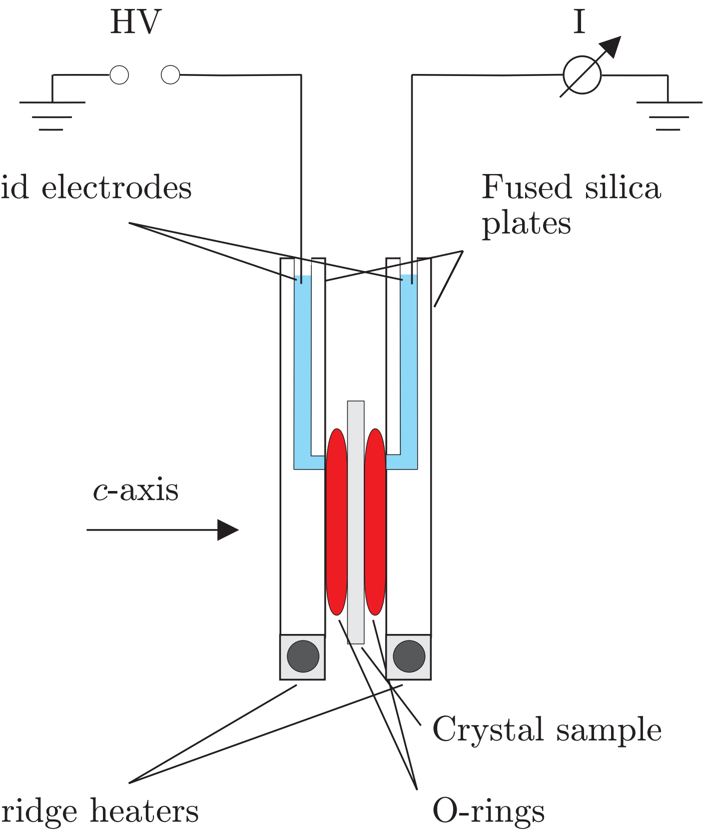

Figure 3.1: Schematic drawing of the sample holder that enables simultaneous heating and UV illumination. The z-cut sample is clamped between two fused silica plates and can be contacted by different sorts of liquid electrodes 3.2. HV: high voltage source, I: ampere-meter.

generated after application of several subsequent pulses.

3.2.3 Heating of the sample

To heat the crystal that is clamped into the sample holder, up to temperatures of 520 K, four cartridge heaters with an overall power of 200 W can be inserted into the metal frame of the sample holder. A temperature sensor located 1 cm from the O-ring on the inner side of the fused silica plate measures the actual temperature of the sample, and a temperature controller enables heating of the sample between room temperature and 520 K with an accuracy of ±1 K. The sample is heated and cooled at a rate of 5 K/min to avoid pyroelectric self-poling [94].

At temperatures above the boiling temperature of water, which is used as the standard liquid electrode for EFP at room temperature, alternative liquid electrode materials have to be used, which should also transmit visible and UV light for simultaneous in-situ visualization and EFP. The high-temperature electrodes used are a saturated calcium dichloride solution (up to 400 K) and then a molten binary salt mixture of potassium nitrate and lithium nitrate (up to 520 K). Both materials have a high conductivity and a sufficient UV transmission at 351 nm. For the intermediate temperature regime, cinnamyl alcohol is used, which, due to its organic nature, does not transmit UV light. All electrodes, their temperature regime of application and the UV transmission through 1 mm of the electrode, which corresponds to the width of one liquid electrode inside the sample holder, are listed in table 3.2.

Type of electrode	Temperature [K]	Transmission [%]
H_2O	290 - 350	100
$H_2O + CaCl_2$	350 - 400	100
Cinnamyl alcohol	400 - 430	0
$LiNO_3 + KNO_3$	430 - 520	40

Table 3.2: Liquid electrodes, used in different temperature regions and their UV transmission at 351 nm wavelength for 1 mm interaction length.

3.2.4 Homogeneous UV illumination of the sample

It is known that homogeneous illumination with weakly absorbed UV light reversibly reduces the coercive field strength of magnesium-doped

$LiNbO_3$, leads to increased uniformity on the growth of the domains [54] and increases the photo-conductivity of the crystal [54, 63]. At room temperature the 334 nm line of an argon-ion laser (Coherent INNOVA Sabre 25/7) is used to illuminate the crystal, since the effect of this wavelength on the poling behavior of MgCLN has been extensively studied [30]. The absorption coefficient at this wavelength is $\alpha < 0.1\,\mathrm{mm}^{-1}$ [30], so the UV light intensity inside the 500-µm-thick crystal can be assumed to be effectively constant. For EFP at elevated temperatures, the 351-nm-line of the argon-ion laser is used for illumination, since the liquid electrodes have a higher transmission at this wavelength (see Tab. 3.2).

One aim of the UV illumination is to utilize the E_C-lowering effect in combination with the structured photoresist to fabricate bulk domain patterns with period lengths in the regime of a few µm. Magnesium-doped samples (MgCLN and MgSLN) are coated with the structured photoresist on the $+z$ face (see Sec. 3.2.2), clamped into the crystal holder and illuminated with UV light of 334 nm with an intensity of $0 - 50$ mW/cm^2 (see Fig. 3.2). High-voltage pulses designed on the basis of pulses used by Caballero-Calero et al. [95] are successively applied with increasing magnitude until the in-situ visualization and monitoring of the poling current indicate a good duty cycle of the domain pattern.

Another aim of the UV illumination is to utilize its effect on the electronic conductivity of the crystal to investigate the impact of the screening of defect clusters on the poling behavior. Here E_C and the internal field of MgCLN crystals are investigated for different UV intensities. Furthermore, heating (see Sec. 3.2.3) and homogeneous UV illumination are combined during EFP, since they increase the ionic conductivity and the electronic conductivity, respectively, and their impact on E_C is investigated. The E_C measurements are conducted with CLN and MgCLN samples, and the hysteresis loop is recorded by plotting the transferred charge vs. the applied field as a function of the applied field (see Sec. 2.2.1). Additionally, the susceptibility of vacuum-annealed CLN samples (see Sec. 3.1) to coercive field reduction by UV light (351 nm), i.e., whether different UV light intensities change E_C, is investigated.

3.3 Domain inversion and domain imaging – measurement of the coercive field strength

The coercive field depends on various intrinsic and extrinsic parameters (see Sec. 2.2.1). Since domain inversion is a stochastic process [96], E_C even

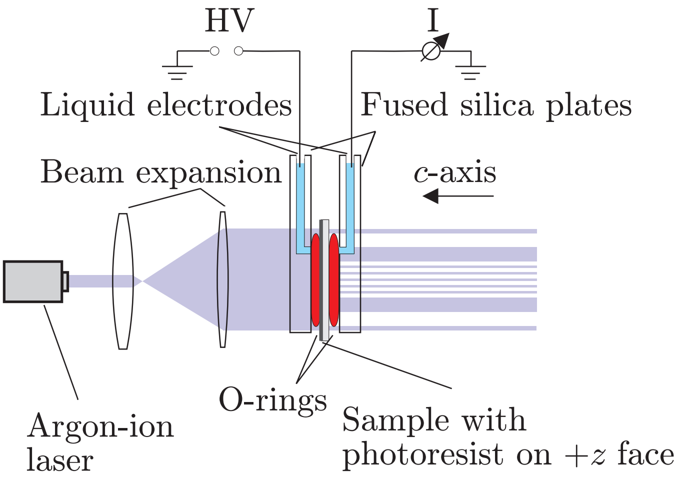

Figure 3.2: Experimental setup for electric field poling with simultaneous UV illumination by an argon-ion laser. Magnesium-doped samples are coated with UV-absorbing photoresist on the $+z$ face to fabricate bulk domain patterns.

depends on the speed at which the electric field is ramped up. Therefore, to obtain comparable data sets, a consistent method for the determination of E_C is crucial.

3.3.1 Inversion of ferroelectric domains

After the sample has been mounted into the sample holder, both z-faces are contacted by liquid electrodes. If EFP is performed at elevated temperatures, the two faces are grounded during heating to prevent the build-up of pyroelectric fields. If not stated otherwise, in all experiments the applied electrical field is increased linearly at $30\,\mathrm{V/(mm\,s)}$, until domain inversion starts at a certain field strength and the poling current can be detected.

3.3.2 Poling current

The poling current I during EFP results from the temporal evolution of the spontaneous polarization and the compensation charges on the z-faces (see Eq. 2.3). For $LiNbO_3$, this current is typically larger than 1 µA for the domain-inverted area of $0.64 - 0.71\,\mathrm{cm}^2$, resulting from the standard-size O-rings. The dark conductivity of all types of $LiNbO_3$ samples used (CLN, MgCLN, SLN, MgSLN), leads to a current which is typically in the regime of 10^{-9} A and is low enough that a distinct poling peak can be observed from this background current. As long as the background current is negligible, for our experiment, E_C is defined as the value of the externally applied field at which the I becomes larger than 1 µA. For all types of $LiNbO_3$, at elevated temperatures the ionic conductivity and in the case of Mg-doped $LiNbO_3$ also for illumination with weakly absorbed UV light the electronic conductivity increases.

3.3.3 In-situ visualization

Figure 3.3 shows the experimental setup that is used to visualize domains during EFP. Collimated light from a cold light source is polarized, then transmitted through the crystal. The second polarizer is set to minimum transmission and the parallel light beam is focussed on a CCD camera to image the entire crystal surface inside the O-ring. The beam from the cold light source can be superimposed with the weakly absorbed UV light by a dichroic beam splitter and all liquid electrodes used for EFP at different temperatures are transparent, so in-situ visualization is applicable for all poling conditions. The birefringence at the domain walls can be visualized while performing EFP (see Sec. 2.2.4) and the nucleation of domains as well as the movement of the domain walls can be imaged.

If the background current during EFP, e.g. at elevated temperatures, becomes too high to precisely determine E_C from the poling current, an alternative method has to be used. Since the EFP setup with liquid electrodes enables in-situ visualization, the field strength at which not only single nucleation spots but domain wall movement all over the crystal can be observed is chosen. This also coincides with the detectable poling current peak for the case of low underground current. These two definitions used here, are related anyway by Eq. 2.3, since the visualized domain wall movement corresponds to the term "$\mathrm{d}A/\mathrm{d}t$" and the poling current is equivilant to "$\mathrm{d}Q/\mathrm{d}t$".

3.3.4 Domain-selective etching

The domain patterns are translated into a topography pattern by domain-selective etching by an aqueous solution of hydrofluoric acid (48%) (see Sec. 2.2.4). Small droplets of hydrofluoric acid (HF) are pipetted on the crystal surface and after the corresponding etch time are neutralized by saturated calcium hydroxide solution: $2\,\mathrm{HF} + \mathrm{Ca(OH)_2} \rightarrow \mathrm{CaF_2} + \mathrm{H_2O}$. The z-faces are etched for 15 minutes, whereas the y-faces, due to their

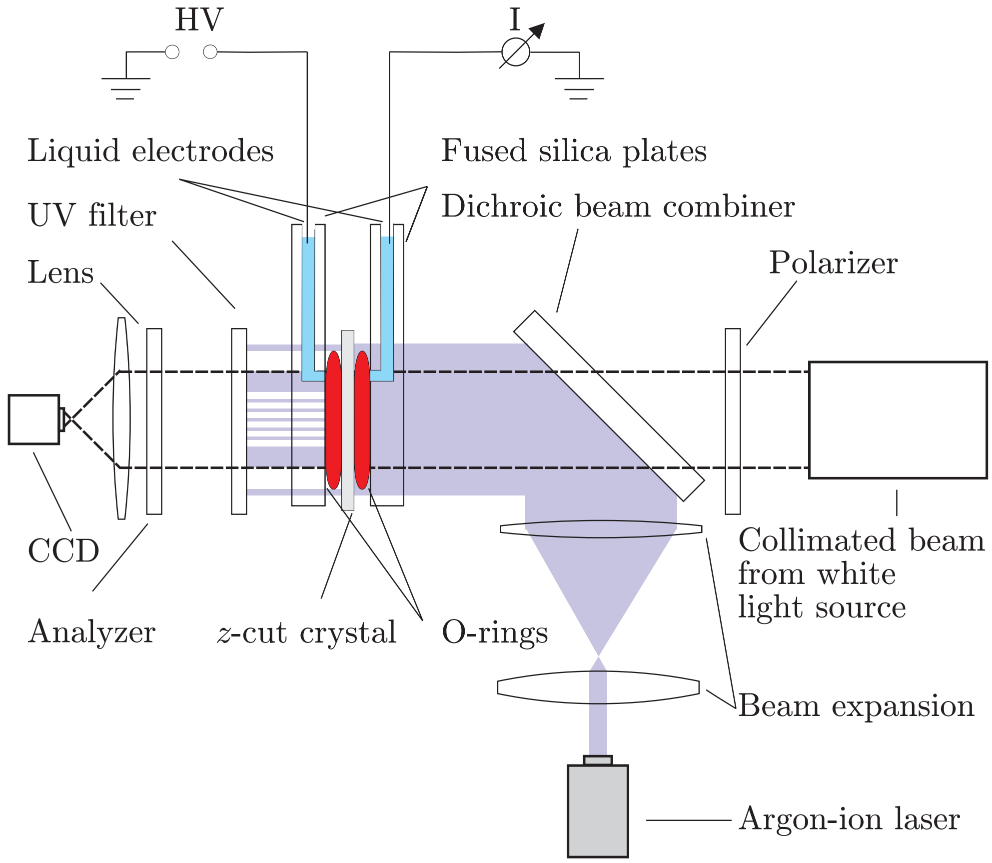

Figure 3.3: Schematic setup for in-situ visualization of domain walls during electrical field poling. The stress-induced birefringence at the domain walls is visualized through crossed polarizers. A dichroic beam combiner enables superposition of the light from the white light source with the expanded UV laser beam, so that the domain growth during UV-assisted electrical field poling can be observed.

lower etch rate, are etched for 1 h, leading to an etched profile height of several 100 nm. The domain pattern is then be visualized by an optical microscope.

The fact that the Rayleigh length of the optical microscope used is smaller than the crystal thickness of 500 µm is utilized to investigate bulk domain patterns: The sample under the microscope is illuminated from the rear, a domain pattern on the $+z$ face, which faces the microscope objective, is imaged and then the crystal is translated towards the microscope objective, i.e. the $+z$ direction until the focus is on the rear face of the sample. So the focus is shifted to the spot on the $-z$ face of the sample with the same x- and y-coordinates and therefore imaging of the same spot on the $+z$ and $-z$ face is enabled. By this method, it can be verified, whether domain patterns grow as bulk domain patterns throughout the crystal or whether they merge, while they grow from the $+z$ to the $-z$ face.

3.3.5 Imaging and generation of domains via piezoresponse force microscopy

A method for domain imaging and domain generation is offered by piezoresponse force microscopy. For domain imaging, an oscillating voltage is applied to the metallized tip of a scanning force microscope [80, 89]. The oscillating voltage induces a thickness oscillation of the crystal via the inverse piezoelectric effect, which is detected by a laser beam reflected by the cantilever (see Fig. 3.4). The amplitude of the oscillating voltage is $5-15\,\mathrm{V}$ peak-to-peak and its angular frequency is in the range of $5-50\,\mathrm{kHz}$, which is less than the cantilever resonance frequency ($>$ 100 kHz) or the resonance frequency of the crystal (GHz regime) [80]. A major advantage of the PFM is that, despite all other methods, it can image domains on the non-polar x-faces [97], which cannot be done by differential HF-etching.

Also an alternative method for ”global” domain inversion performed by EFP, namely ”local” domain inversion by application of a voltage to the tip of a scanning force microscope in contact mode in $LiNbO_3$, is offered by the PFM [76, 98]. The sharp PFM tip ($\approx$ 50 nm tip radius) yields a divergent electric field, which has an electric field strength near the tip that exceeds the coercive field strength even for application of moderate voltages ($\approx$ 100 V) to the tip [80].

For PFM poling a z-cut MgCLN crystal has to be thinned down to less than 30 µm and is grounded on the rear side. Then the voltage is applied in contact mode and a locally domain-inverting field is generated. Either small domain hexagons in the nm-regime can be generated by application of short voltage pulses in the ms-regime [76] or alternatively, serial lines, with a width around 100 nm, can be poled by scanning the surface under a constant voltage [99].

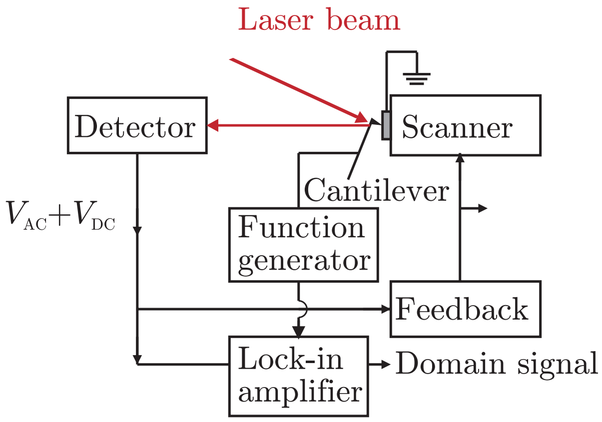

Figure 3.4: Schematic of a piezo force microscope (PFM), replotted from [80]. An oscillating voltage (V_{AC}) and a constant voltage (V_{DC}) can be applied to the tip for either probing the domain structure or generation of domains. The rear side of the sample is grounded. The domain signal is detected by a lock-in amplifier, operating at the frequency of V_{AC}.

3.4 Domain patterning by local irradiation with strongly absorbed UV light

An alternative method for domain structuring in lithium niobate is poling inhibition (PI) [78]. To achieve PI, the $+z$ face of a crystal is irradiated with a tightly focussed, strongly absorbed UV laser beam. The irradiated locations maintain their polarization during subsequent EFP, indicating that the local coercive field is significantly increased. Both, the lateral width and the depth of the generated domains, is on the micron scale [90]. The applicability of PI has been confirmed by Sones et al. in CLN and MgCLN [78]. In the following it will be investigated if PI works in stoichiometric material, as well.

3.4.1 Irradiation setup

The beam of an argon-ion laser operating at a wavelength of 275 nm is focussed on the $+z$ face of the crystal (see Fig. 3.5). The room temperature absorption coefficient α of the UV light is more than 1 µm^{-1} for all materials investigated [31, 33]. The sample is mounted on a two-dimensional translation stage (Micos SMC-corvus) which has an absolute accuracy in translation of 30 nm for both axes. The optical axis of the UV laser beam is perpendicular to the translation axes, so that the focus of the beam can be scanned across the surface of the crystal. The beam, with a TEM$_{00}$ mode, is focussed by a fused silica lens with a focal length of 37.5 mm to a spot with focal radius of (2.5 ± 0.75) µm (at FWHM). All types of z-cut crystals listed in table 3.1 were used to investigate the impact of stoichiometry and MgO-doping on PI.

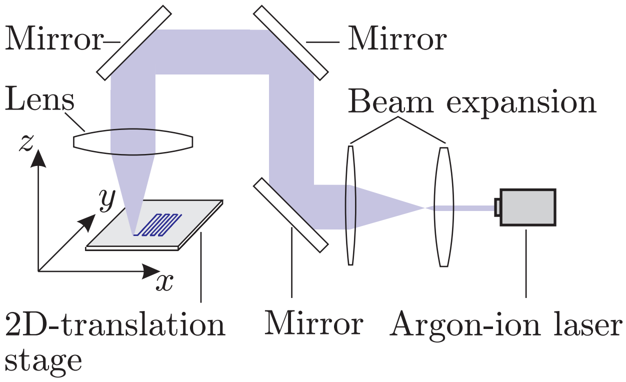

Figure 3.5: Schematic of the setup for local irradiation of the crystal surface with strongly absorbed UV light. The expanded UV laser beam of 275 nm is focussed on the crystal surface by a lens (focal length: 37.5 mm) to a spot with a focal radius (FWHM) of $r_0 = (2.5 \pm 0.75)$ µm. By movement of the computer-controlled 2D translation stage, arbitrary trajectories can be scanned on the sample surface.

The previously described setup enables generation of arbitrary patterns of parallel UV-irradiated lines or dot arrays. A desirable application of PI domains, namely whispering gallery mode resonators (WGRs), requires a radial domain structure to achieve a constant period length for the light propagating inside the WGR. To scan a radial pattern on the crystal surface, a computer-controlled precision rotation stage (Newport RVS80) is mounted on top of the translation stage. With the aid of a computer controlled algorithm, a radial latent state (LS) pattern with a diameter of 6 mm is generated on the $+z$ face. The mounted crystal is already attached to the metal cylinder used for the fabrication process of the WGRs by diamond turning, so the center of the radial structure differs from the center of the WGR by only several µm.

3.4.2 Generation of the latent state

The fabrication of PI domain patterns can be divided into two steps, namely the irradiation of the crystal with UV light and subsequent EFP of this crystal. It is evident that the crystal properties are strongly altered in the UV-irradiated areas, even though no domain reversal has yet been observed. This changed state of the crystal, referred to as *latent state*, is the cornerstone of the PI phenomenon. The latent state was found to be very stable under ambient conditions [100] – no effect of the time interval between the primary UV irradiation and the subsequent EFP was observed. Extensive iteration of parameters including scanning velocity v, which describes how fast the laser focus is moved across the surface and the laser power incident on the surface P_{UV} has been performed [24, 100]. Ying et al. found that for a scan velocity $v = 100\,\mu\mathrm{m/s}$ and laser powers between 35 and 45 mW, which correspond to a UV intensity of $I_{\mathrm{UV}} \approx (1.8 - 2.3) \times 10^5\ \mathrm{W/cm^2}$, with an accuracy of $0.5 \times 10^5\ \mathrm{W/cm^2}$, the best results for PI could be achieved in terms of uniform domain structures and minimum thermal damage [100]. One aim of the experiments conducted is to understand the mechanism of formation and the properties of this LS. It will be investigated, if the LS is attributed to structural changes – to local changes in stoichiometry or to e.g. the concentration of point defects. Potentially however it could also be linked to internal space-charge fields caused by UV-induced charge separation.

Note that for strongly absorbed UV light of a wavelength below 306 nm the resulting PI domains do not significantly depend on the wavelength used, i.e., in our case the different emission lines of the Ar-ion laser (305.5, 302.4, 300.3 and 275.4 nm), in terms of surface damage and domain quality [100]. Only the depth of the PI domains slightly increases for shorter wavelengths. In this thesis all experiments with strongly absorbed UV light are performed with light of wavelength 275.4 nm.

3.4.3 Poling inhibition

After the latent state is written on the crystal surface, the sample is mounted in the crystal holder and is domain-inverted three times by EFP, since it was found that this results in continuous surface domain structures [100]. The applied field is ramped up with a rate of 30 V/(mm s) until the domain inversion process starts. This is determined by monitoring the stress-induced birefringence originating from the domain boundaries and when the poling current exceeds the threshold of 1 µA. Then the applied field is kept constant until the poling current drops below the threshold of 1 µA, and then the field is ramped down. This procedure enables slow and smooth domain wall propagation, which was found to effectively translate the LS into a domain pattern. The resulting PI domains can be investigated either by PFM or by HF-etching.

3.4.4 Persistence of the latent state

Closer investigation of the LS is performed to clarify the driving mechanism for PI. Since the LS is stable under ambient conditions, the stability of the latent state under either homogeneous illumination with weakly absorbed UV light or annealing of the crystal is investigated. Each sample underwent one of three treatments prior to EFP: annealing at temperature $T = 520$ K for one hour, annealing at $T = 670$ K for one hour, or uniform illumination with weakly absorbed UV light at 334 nm for 30 min (intensity: $I_{334\,\mathrm{nm}} = 150 \pm 5\ \mathrm{mW/cm^2}$).

The chosen annealing temperatures correspond to different charge transport mechanisms: most likely only protons are relevant at $T \approx 520$ K, whereas Li ions become mobile enough at $T \approx 670$ K to significantly contribute to the ionic conductivity [101]. It is known also that the photoconductivity becomes strong in MgCLN upon weakly absorbed UV irradiation with light of a wavelength of 334 nm, compared to the initial dark conductivity [30].

3.4.5 Irradiation of the non-polar faces

The effect of direct domain writing on the $-z$ face [77] and poling inhibition for the $+z$ face [78] is already known for the irradiation parameters described in section 3.4.2. The same irradiation procedure is now applied to the x- and y-faces of $LiNbO_3$ [CLN(y) and MgCLN(x)]. To investigate the impact on the domain structure for the y-face, differential etching can be applied but since the two x-faces do not exhibit differential etching rates, PFM has to be utilized to image domain structures [97].

After UV-irradiation, the non-polar faces of some crystals are carefully polished . Due to the thermal surface damage of the UV-irradiated tracks, the laser-written lines can be seen as a corresponding topographical image with a depth of several nanometers, by PFM.

Chapter 4

Experimental results

4.1 Domain patterning with structured electrodes and ultraviolet light illumination

In this section the results of domain patterning using structured electrodes are summarized. In addition to the structured electrodes, spatially modulated illumination with weakly absorbed UV light at 334 nm is used to pattern the coercive field reduction and to generate a bulk domain pattern (see Sec. 3.2.4). Since coercive field reduction by illumination with light of 334 nm only works with Mg-doped lithium niobate [54], only MgCLN and MgSLN crystals are processed and investigated by optical microscopy after HF etching.

4.1.1 Domain patterning in Mg-doped congruent lithium niobate

The MgCLN samples are clamped into the crystal holder and homogeneously illuminated with UV light on the $+z$ face. The duration of the HV pulses, the pulse amplitude and the UV intensity $I_{334\,\mathrm{nm}}$ are varied respectively, and the resulting domain patterns were evaluated. Iteration of these three parameters yields reasonable domain patterning on the $+z$ face (peak amplitude: 24 kV/cm, pulse duration: 200 ms, $I_{334\,\mathrm{nm}} = 40\,\mathrm{mW/cm^2}$) but on the $-z$ face, the domains are merged and the pattern is not preserved for all period lengths between 6 μm and 50 μm. The resulting domain pattern on both faces for a period length of 10 μm is shown as an example in Fig. 4.1. On the $+z$ face the electrode pattern with a duty cycle of 0.1 is translated into a domain pattern with a duty cycle around 0.5 but on the $-z$ face the domains at the same spot are merged to hexagons and no domain pattern can be observed. Even for the larger period lengths up to 30 µm the domains merge as they grow from the $+z$ to the $-z$ face.

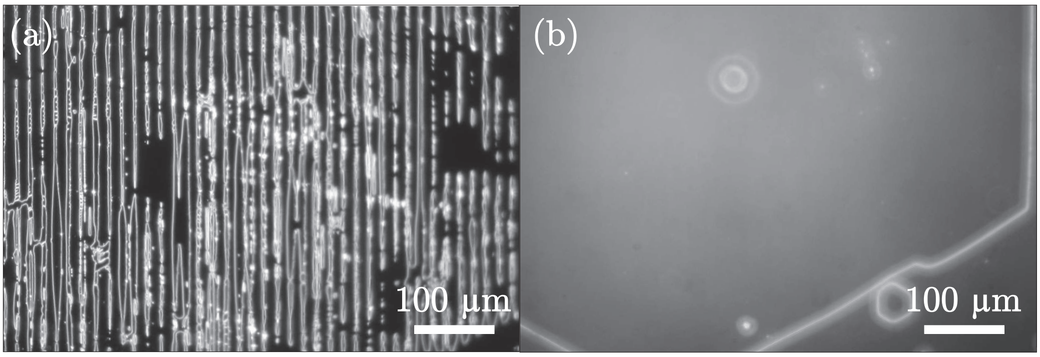

Figure 4.1: Typical domain structure obtained for EFP with successive HV pulses in MgCLN with simultaneous homogeneous illumination with UV light of 334 nm wavelength. The structured electrode pattern on the $+z$ face is translated into (a) a domain pattern with a duty cycle of 0.5. The domain pattern does not grow trough the entire crystal: (b). On the $-z$ face only hexagonal-shaped merged domain structures are observed.

4.1.2 Domain patterning in Mg-doped near-stoichiometric lithium niobate

The mechanism of reversible coercive field reduction has been already reported for near-stoichiometric, magnesium-doped $LiNbO_3$ as a proof of principle by Wengler et al. [30]. To obtain suitable illumination parameters, the dependence the coercive field on UV illumination for different intensities (E_C^λ) is measured. The results for a wavelength of 334 nm are shown in Fig. 4.2. A UV intensity of $I_{334\,\mathrm{nm}} = 30\,\mathrm{mW/cm^2}$, where the E_C^λ is reduced to 50% of the value of $E_C = 3\,\mathrm{kV/mm}$, is set as a reasonable starting point for the iteration of domain patterning for different samples at different UV intensities.

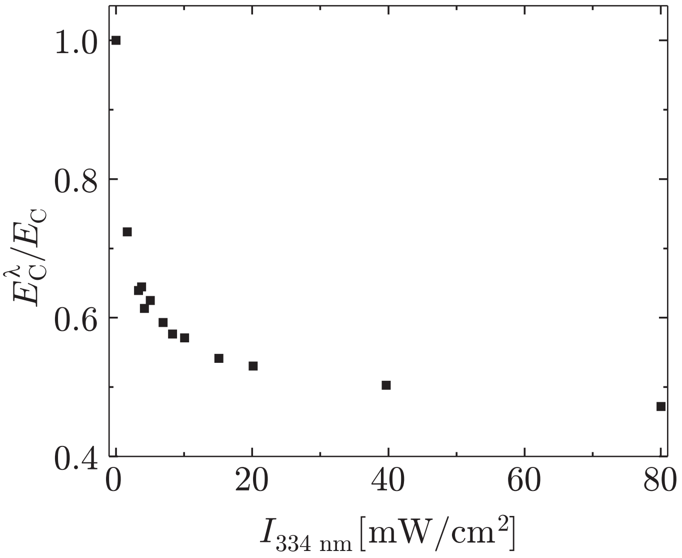

Figure 4.2: Coercive field strength (E_C^λ) vs. the intensity of the UV light incident on the $+z$ face of MgSLN. Here E_C^λ is normalized to the initial coercive field strength (E_C), which is measured without UV illumination.

The duration of the pulses, the pulse amplitude and the UV intensity $I_{334\,\mathrm{nm}}$ are varied, and the best result is obtained for the following parameters: $I_{334\,\mathrm{nm}} = 40\,\mathrm{mW/cm^2}$, a pulse amplitude of 3 kV/mm and a pulse duration of 300 ms. A typical HV pulse and the resulting poling current, indicating structured domain growth, are depicted in Fig. 4.3. Microscope images of both faces of the etched crystal are shown in Fig. 4.4 and clearly indicate that a bulk domain pattern is generated in the MgSLN crystal, which has mostly a duty cycle close to 0.5 and some part with merged domains.

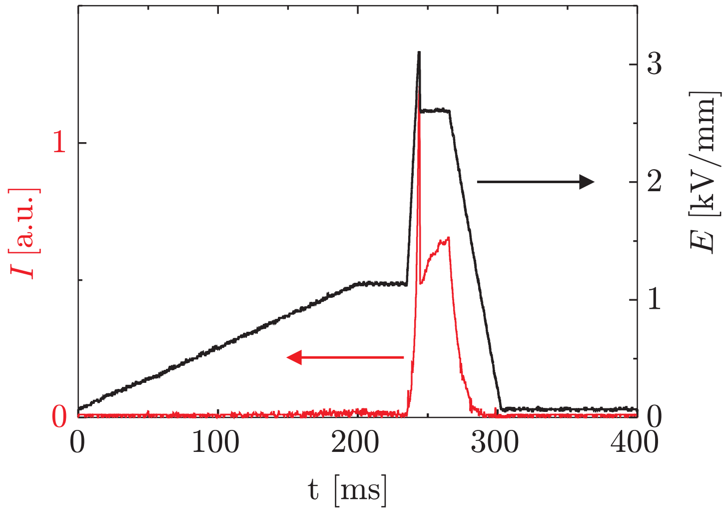

Figure 4.3: Applied HV pulse and the poling current versus time for MgCLN homogeneously illuminated with UV light ($I_{334\,\mathrm{nm}}$ = 40 mW/cm^2; E: externally applied electric field; I: electrical current). The non-ohmic behavior of the current (between t= 250 ms and t= 300 ms) indicates that the current results not from conductivity but from redistribution of compensation charges.

The same poling procedure is performed with another coated MgSLN crystal but without UV illumination. In this case, a domain pattern on the $+z$ face is generated. However, it does not penetrate through the crystal, i.e., no pattern on the $-z$ face is obtained. Furthermore, a crystal with homogeneous illumination from the $-z$ face, i.e., the uncoated side, was processed with the same parameters. After HF etching no domains that have the shape of the photoresist pattern could be found, but only domains of the typical hexagonal shape, which confirms the impact of the structured UV illumination on the generation of bulk domain patterns.

4.2 Domain patterning by UV irradiation

An alternative, serial method for domain patterning is offered by poling inhibition. In contrast to EFP with structured electrodes, where the field which is applied to the crystal is locally modulated by a structured photoresist, in the case of PI the EFP step is performed with a homogeneous

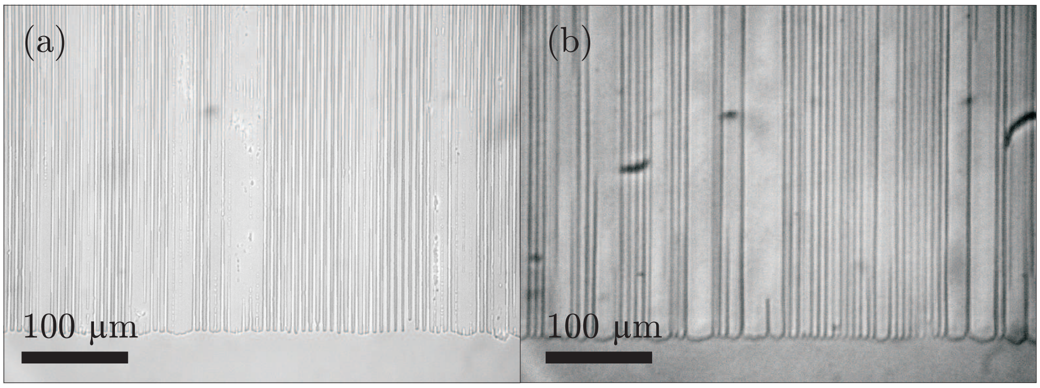

Figure 4.4: Typical domain structure obtained for EFP with subsequent HV-pulses in MgSLN and simultaneous homogeneous illumination with UV light of 334 nm wavelength. The structured electrode pattern on the $+z$ face is translated into a bulk domain pattern with a duty cycle close to 0.5 (a). Only few domains merge, and the domain pattern can be observed on the $-z$ face, as well (b).

electric field, but the UV-irradiated areas of the crystal do not reverse their spontaneous polarization, when the applied field exceeds E_C.

4.2.1 Poling inhibition in near-stoichiometric lithium niobate

Samples of SLN and MgSLN are irradiated with UV light using the standard parameters and the experimental setup described in Sec. 3.4.2. A pattern of 24 laser-irradiated tracks with a spacing of 20 μm and a length of 12 mm is written parallel to the crystal y-axis with different UV intensities ($I_{\mathrm{UV}} = (1.8 - 2.3) \times 10^5$ W/cm^2) that span the intensity regime for congruent material from no generation of PI to resulting strong surface damage[100].

Then, the samples were poled three times and the resulting domains were examined. Strong thermal damage is observed on the surface for the highest intensity, as in the case of MgCLN and CLN [100], but no PI domain structures could be observed for any intensity. The result for the highest intensity without thermal surface damage is shown in Fig. 4.5. A domain wall can be observed in the lower part of Fig. 4.5, where the region above the domain wall was domain inverted three times. No solid domain structures but only small domain nuclei that have retained their original spontaneous polarization are observed, so the PI mechanism is apparently hampered by a better stoichiometry of the crystals. Thus, in the following,

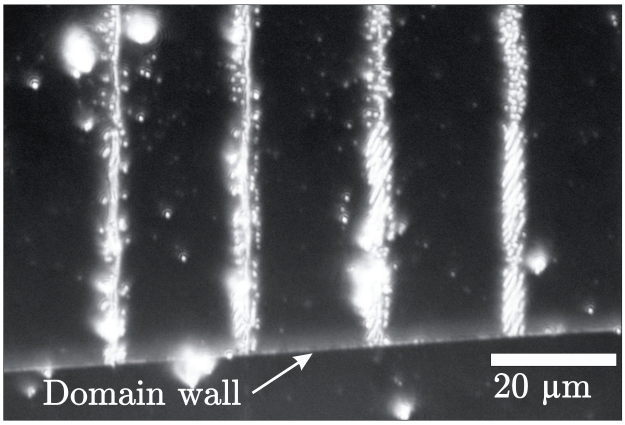

Figure 4.5: Resulting domain structure on the $+z$ face of an HF-etched crystal, obtained for optimized irradiation parameters with regard to surface damage for SLN ($I_{\mathrm{UV}} = 2.4 \times 10^5$ W/cm^2). Only faint domain nuclei but no solid PI structures are observed above the domain wall. In the part of the crystal above the domain wall of the crystal, the spontaneous polarization is oriented antiparallel to the orientation of the spontaneous polarization of the untreated crystal, since an odd number of poling steps has been performed.

only experimental results for PI in congruent material (CLN and MgCLN) will be presented.

4.2.2 Persistence of the latent state

The latent state, which exhibits a high stability under ambient conditions, is generated in MgCLN and CLN crystals. One of the CLN and one of the MgCLN crystals, each undergo one of the treatments described in section 3.4.4 before EFP. The resulting domains are investigated after HF-etching of the $+z$ face, and the results are summarized in Tab. 4.1. Annealing at 520 K for 1 h as well as treatment with weakly absorbed UV light do not affect the LS – poling inhibition occurs just as in non-treated samples. However, the higher temperature annealing (670 K) eliminates the LS – poling inhibition does not occur. This behavior was found to be independent of both the type of the crystal used (CLN or MgCLN) and the UV laser power utilized initially to create the latent state.

	1 h at 520 K	1 h at 670 K	30 min at 334 nm
CLN	No effect	Elimination	No effect
MgCLN	No effect	Elimination	No effect
Mobile species	H^+	H^+ and Li^+	e^-

Table 4.1: Experimental results on the effect of intermediate treatments (annealing and illumination) on poling inhibition. The mobile charge carriers for the different treatments are protons (H^+), lithium ions (Li^+) and photo-excited electrons (e^-) [30, 101].

4.2.3 Mapping of the coercive field

Since PI is linked to a local alteration of the coercive field E_C, it is worth examining the local spatial distribution of E_C in the area of the laser-irradiated track. Electric field poling with homogeneously contacting electrodes only allows for ”global” inversion of the spontaneous polarization and therefore does not enable local mapping of E_C, i.e., investigating whether the crystal poles at different field strengths at different positions. A spatial distribution of E_C is indicated, anyhow, since in-situ visualization shows that during the third step of EFP, after the crystal has already been poled and re-poled once, the nucleation of the domains starts right next to the LS area.

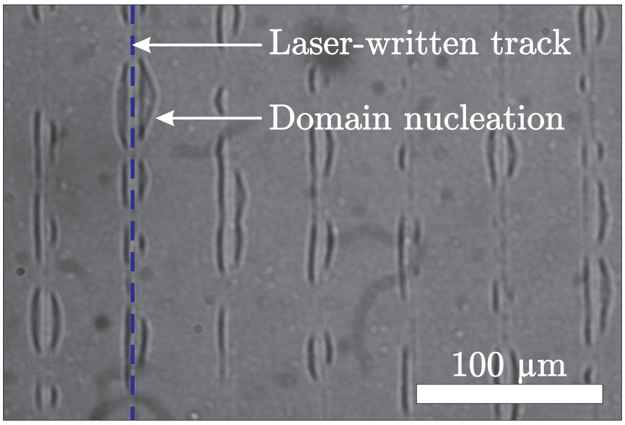

Figure 4.6: Domain nucleation on the $+z$ face of MgCLN next to the latent state, indicating that the coercive field is reduced adjacent to the LS area. One of the laser-written tracks is indicated by a dashed line.

A MgCLN crystal with the LS written on the $+z$ face is only partially poled, i.e., the field is ramped down right after domain nucleation is observed and then the crystal is HF-etched. In Fig. 4.6 it can be seen that the nucleation starts in the area adjacent to the LS, indicating that the coercive field next to the LS is locally reduced.

In order to map even more precisely the spatial distribution of the coercive field, local-poling experiments using a piezoresponse force microscope are performed. A MgCLN crystal, where the LS was inscribed using different laser powers, is thinned down by abrading and polishing of the $-z$ face to a thickness of only 26 µm. Using the setup described in Sec. 3.3.5, a voltage of +100 V is applied to the tip of the PFM, while scanning a 5-µm-high stripe, consisting of 64 scanlines, perpendicularly to the laser-irradiated track (Fig. 4.7). Because of the electric-field enhancement at the very sharp tip, such low voltages are sufficient for poling. The generated domain structures are visualized by PFM.

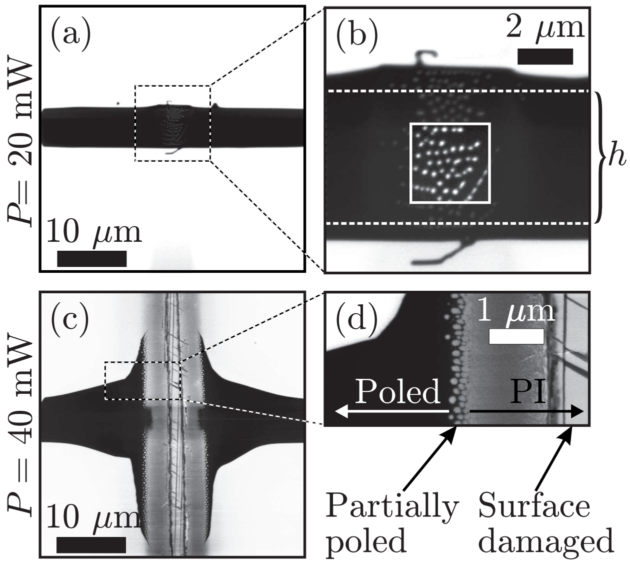

Figure 4.7: Piezoresponse force microscopy images obtained on MgCLN after locally poling a horizontal stripe $h = 5$ µm height with the piezo force microscope tip. For the generation of the LS, vertical laser tracks written with (a) 20 mW and (c) 40 mW power were used. The magnified image (b) shows the generation of nano-poling inhibited domains within the UV-laser-irradiated track. In (d) the formation of nanodomains occurs only at the transition region between poled and poling-inhibited area. In the center of the UV-irradiated track, the surface is strongly damaged. Vertical dimensions in this figure are referred to as height, while horizontal dimensions are referred to as width.

Figure 4.7 shows PFM images obtained after local poling with the PFM-tip across UV-irradiated tracks, written with light of different laser intensities (1×10^5 and 2×10^5 W/cm^2). In Fig. 4.7(a) the result for the lower power is seen, the laser-irradiated track passing vertically through the center of the image. Basically, two contrast levels can be distinguished: bright for the unpoled area and black for the poled area. Poling with the PFM tip was obviously successful within the full 5-µm-high stripe, seen as the horizontal black bar. Upon closer inspection , it can be seen in Fig. 4.7(b) that the poled area has a height that is slightly larger than 5 µm , thus sideways domain growth has occurred. As for the quality of the poling within the UV-irradiated area, it is found to be imperfect , showing an assembly of nanometer-size features of different contrast indicating local resistance of poling, in effect nano-domains. This can be best seen in the area within the white square, where the image contrast is enhanced by using image processing software.

For the higher laser intensity of 2×10^5 W/cm^2, the situation is different [Fig. 4.7(c)]. The image basically shows three contrast levels: bright and dark for unpoled and poled areas, respectively, and in addition a gray level along the UV-irradiated track. Figure 4.7(c) shows a clear broadening of the PFM-poled region in the vicinity of the UV-irradiated track, Although the PFM-scanned stripe maintained a height of 5 µm along the sample, the height of the actual area appears to be a function of proximity of the UV-irradiated track. However, no contrast change could be observed on the UV-irradiated track, which is an indication that no poling occurred there. This poling behavior indicates an increase of the coercive field along the UV-irradiated track. This is also accompanied by an E_C reduction in the adjacent region as indicated by the broadening of the PFM-poled stripe.

The PFM signature of the PI area, i.e., the grayish area, needs further description. It can be subdivided into a central part of approximately 2.5 µm width, showing indications of direct UV-induced surface damage, an adjacent 3-µm-wide region, where the crystal structure was only marginally affected by the laser irradiation, and a partially poled transition region, where nanodomains emerge [Fig. 4.7(d)]. The depth of the UV-laser-inflicted surface damage is on the order of 100 nm [90]. Since the gray level of the PFM image within the UV-irradiated track is bright rather than black, it is concluded that this area has also resisted poling; the reduced piezoelectric response results from the surface damage.

4.2.4 Bulk domain patterning by poling inhibition

At sufficiently high intensities that still lie below the threshold of strong thermal damage ($I_{\mathrm{UV}} = 2 - 2.3 \times 10^5$ W/cm^2), the LS of MgCLN can be converted into a bulk domain pattern by two subsequent EFP steps. For CLN, so far only PI domains with a depth of less than 2 µm have been produced [90]. It is found that at these relatively high UV light intensities, after the first EFP poling step, during repoling, a strong current signal during EFP is observed, which can not be attributed to the redistribution of compensation charge carriers, since the integral of the current measured during the poling step is of the order of 10^{-3} C, exceeding drastically the product of the entire contacted area ($A = 0.64 - 0.71$ cm^2) and the spontaneous polarization given by $Q = A \times P_S = (4.5 - 5) \times 10^{-5}$ C.

A typical bulk-domain pattern, obtained for PI with a UV intensity of $I_{\mathrm{UV}} = 2 \times 10^5$ W/cm^2 in MgCLN, is shown in Fig. 4.8. The domains on the $+z$ face show slight thermal damage in between the two domain walls (see Fig. 4.8a). Even though the LS on the $+z$ face is written equidistantly with a spacing of 50 µm, the bulk domains do not grow absolutely straight along the z-axis and the resulting domain pattern on the $-z$ face is not entirely equidistant (see Fig. 4.8b).

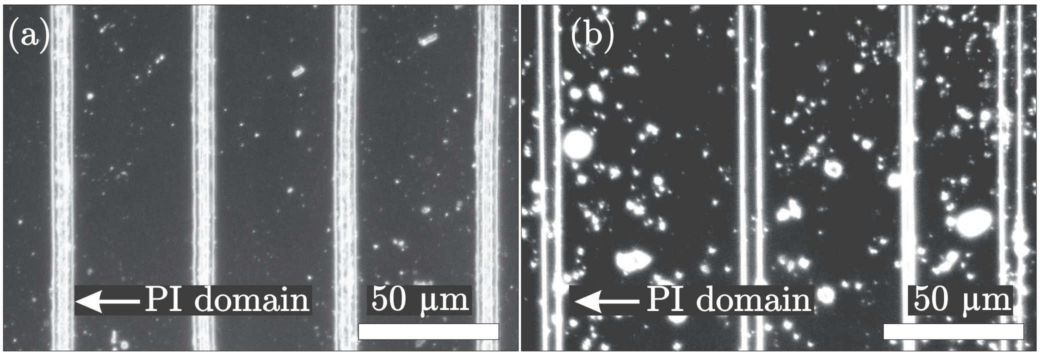

Figure 4.8: PI bulk-domain pattern resulting from two successive poling steps after writing the LS with a UV intensity of $I_{\mathrm{UV}} = 2 \times 10^5$ W/cm^2. The domain walls at the same position on the crystal on (a) the $+z$ face and (b) the $-z$ face, imaged by optical microscopy after HF-etching indicate that bulk domains have been grown from the LS on the $+z$ face. The UV-written tracks were scanned with a spacing of 50 µm parallel to the y-axis of the crystal.

4.2.5 PI domain patterning for whispering gallery mode resonators

An application of bulk domain patterns generated by PI, which can benefit from the specific features of PI domain patterns in the fabrication process are whispering gallery mode resonators (WGRs) [102, 103]. The LS is written on a MgCLN sample that is already mounted on the rod for the subsequent diamond turning and polishing, yielding a good proximity of the center of the radial domain structure and the center of the WGR. This leads to a rather small chirp of the domain period at the fringe of the WGR, enabling a high efficiency for the non-linear optical processes [103].

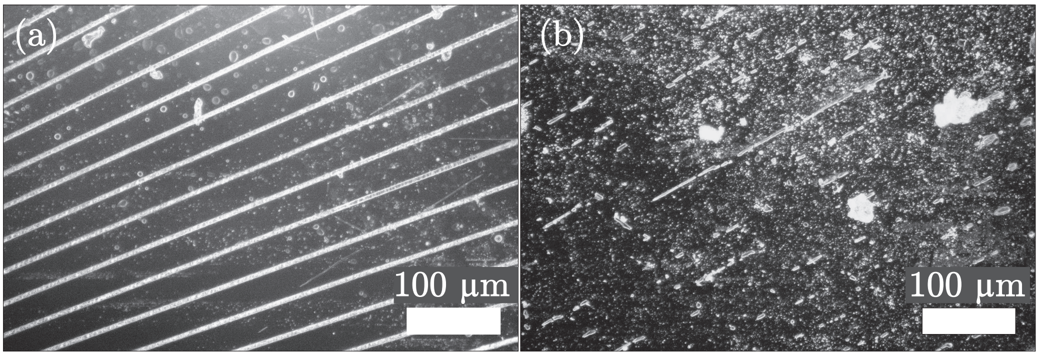

Figure 4.9: Microscope image of (a) the $+z$ face and (b) the $-z$ face of MgCLN patterned with a radial LS pattern (radius of the WGR in the z-plane: 3.5 mm, curvature radius of the fringe of the WGR: 1.5 mm angular spacing of UV-laser-written tracks: 0.9 °). Whereas the $+z$ face shows a domain structure, which corresponds to the UV-irradiated tracks, only few domains that correspond to the UV-irradiated tracks can be seen on the $-z$ face, indicating that only few domain have grown through the entire crystal.

A typical result for a PI domain pattern for the WGRs with a radial domain spacing of 0.9 ° is shown in Fig. 4.9. The radial-symmetric LS pattern is converted into a domain pattern on the $+z$ face (see Fig. 4.9) but only few domains that correspond to the LS pattern can be seen on the $-z$ face.

Since the maximum of the light field of the WGR modes is confined half way between $+z$ face and $-z$ face (see Fig. 4.10), it is crucial to characterize the domain pattern in the middle of the z-cut crystal. Therefore a MgCLN sample containing a bulk domain pattern generated by PI is cut perpendicular to the y-axis, close to the inside radius of the LS structure, and the resulting y-face is polished and HF-etched. The cross section of the radial domain pattern, with a cut distance of 2 mm from the center of the

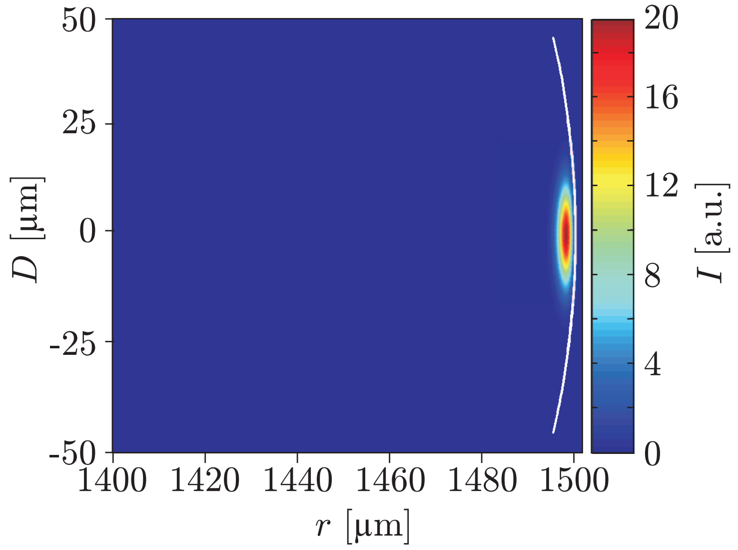

Figure 4.10: Simulation of the light intensity profile of the fundamental mode in a WGR with a thickness of 500 µm and an outer radius $r = 1500$ µm based on the analytic theory of Little et al. [104]. The curvature radius of the fringe of the toroid-shaped WGR, indicated by the white line, is 570 µm. The crystal's z-axis and the electric component of the light field are parallel to the resonators axis of symmetry, i.e., vertical. The origin of the ordinate (D) of the plot is located in the middle of the crystal, therefore in a depth of 250 µm from the $+z$ face. Simulation by Tobias Beckmann.

radial domain structure, is shown in Fig. 4.11. The PI bulk domains have a width of (4.5 ± 0.6) µm at the $+z$ face, get thinner as they grow into the depth of the crystal and most of the domains reach a depth of at least 250 µm. The dashed line, which is parallel to the crystal z-axis, indicates the center of the radial LS pattern. There is a gap without domains under an angle of $(30 \pm 2)^\circ$ from the crystal y-axis, where no PI bulk domains have been generated.

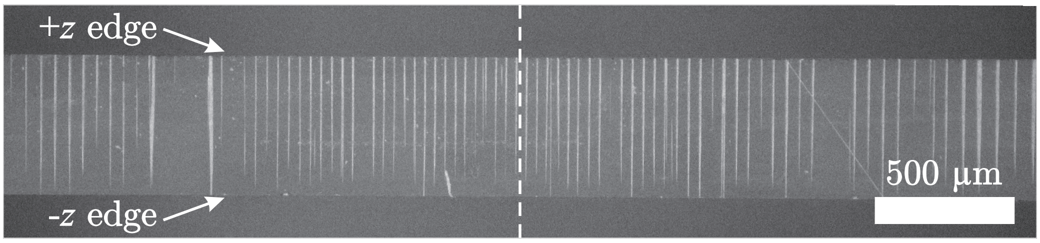

Figure 4.11: The cross section of a radial PI bulk domain pattern inside a MgCLN sample shown on a HF-etched y-face. The PI domains grow from the $+z$ edge into the crystal and most of them reach a depth of at least 250 µm. The symmetry axis, i.e. the axis of rotation during UV laser irradiation, of the radial domain pattern, written on the $+z$ face is indicated by the dashed line.

4.2.6 Direct domain writing on the non-polar faces

Besides the extensively investigated methods of direct domain writing and PI on the $-z$ face and $+z$ face, respectively, the irradiation setup described in Sec. 3.4.1 is also used to irradiate the non-polar x- and y-faces of $LiNbO_3$ and the resulting domain patterns are investigated. Since UV light absorption coefficient and thermal diffusivity do not significantly depend on the crystallographic axes along which they are measured, scanning parameters identical to the parameters for PI are applied to the y-face of CLN(y) and the x-face of MgCLN(x) ($I_{\mathrm{UV}} = (1.8 - 2.3) \times 10^5$ W/cm^2, focal radius at FWHM of (2.5 ± 0.75) µm and scanning velocity of 100 µm/s). Laser tracks were written either parallel, antiparallel, or perpendicular to the z-axis of the crystal, denoted later as $v \rightrightarrows z$, $v \leftrightarrows z$, and $v \perp z$, respectively. Since the etching rate of the y-faces is low and the x-faces do not exhibit any HF-etching at all (see Sec. 3.3.4), the laser-irradiated samples are subsequently investigated by PFM to reveal the generated domain patterns.

Figure 4.12 shows the result of a UV-irradiated track, written along the y-direction on an x-cut sample. The bright portion of the track in the PFM image of Fig. 4.12(a) corresponds to a laser-written domain. The simultaneously obtained surface topography image in Fig. 4.12(b) reveals that the width of the inverted domain is only approximately half of the width of the UV-irradiated track. The latter manifests itself as a shallow indentation, of 6 nm depth, on the surface, owing to the brief polishing step, which more efficiently removes the part of the crystal damaged by the strong laser irradiation. Furthermore, the proliferation of the scratches in Fig. 4.12(a), caused by thermally induced cracking owing to the irradiation procedure, confirms that the width of the laser beam was twice as large as the width of the domain-inverted area. The PFM- and the topography line scan in Fig. 4.12(c) show that only the right half of the laser-irradiated track, i.e., the half pointing into the original $+z$ direction of the crystal, is domain-inverted. This characteristic is confirmed by the presence of the thermo-induced damage due to the irradiation procedure across the full width of the irradiated track, which manifests itself as lines along the three equivalent y-axes. For scanning perpendicular to the z-axis on the y-faces of CLN(y) an analogous domain structure is formed with the half of the irradiated track pointing towards the initial $+z$ direction being domain inverted.

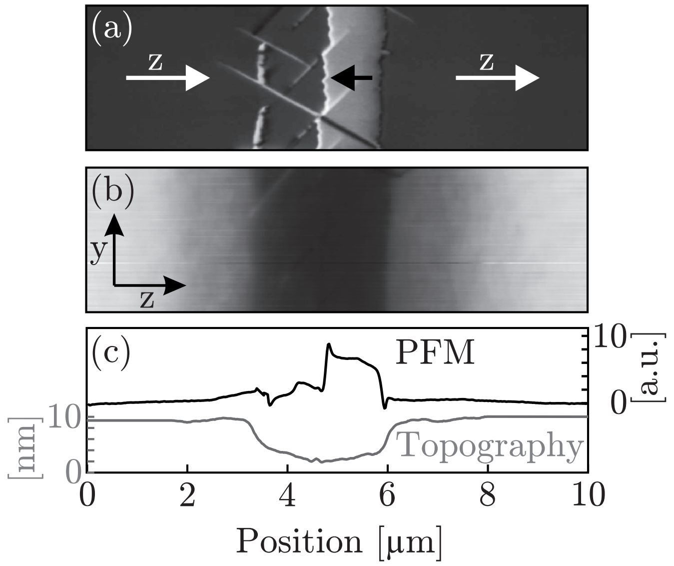

Figure 4.12: Piezoresponse force microscopy image (a) and simultaneously recorded topography (b) of an Mg-doped x-cut $LiNbO_3$ crystal [MgCLN(x)], previously irradiated with a UV laser beam along the y-axis. As best seen by the line scans in (c), a domain of half the width of that of the focused laser beam has been generated. The scratches in (a) are thermo-induced cracks.

To investigate the impact of the scanning direction of the UV laser light with regard to the crystallographic axes, first a pattern with lines perpendicular to the z-axis on a CLN(y) crystal is generated and then lines parallel and antiparallel to the z-axis are scanned. Figure 4.13(b-d) shows PFM images, where laser writing has been performed along the x- and z-directions with standard PI scanning parameters. The laser tracks are numbered in chronological order by ① to ④.

Obviously when moving the laser beam along the x-axis, and thus perpendicular to the z-axis ($v \perp z$; ① and ②) domains of half the width of the laser beam are generated, and the direction of the laser beam movement has no influence on the generated domains. When moving the laser beam parallel to the z-axis, either a domain of the full width of the laser beam is generated ($v \leftrightarrows z$; ④) or no domain at all emerges ($v \rightrightarrows z$; ③). Note that previously written domains (from the laser tracks ① and ②) are erased, since the spontaneous polarization is reoriented into its original direction, during laser irradiation along track ③ [see Fig. 4.13(c)].

In order to gain further understanding of the underlying experimental mechanism, a series of additional experiments was carried out and the results are briefly summarized in the following: (i) the x- and the y-faces show the same poling behavior, (ii) the width of the domains was found to decrease with decreasing laser power (keeping the focussing constant), (iii) their depth was measured to be of the order of few microns, (iv) with strongly reduced laser intensity (by a factor of two), poling was no longer observed, and (v) poling works for both CLN and MgCLN crystals, which is an important issue in terms of applicability of this technique.

4.3 Influence of heat and UV light on the coercive field

The aim of the E_C measurements for different temperatures and UV light intensities, described in Sec. 3.2.4, is to compare the two transient, reversible mechanisms to reduce E_C, by heating and ultraviolet light illumination, and to identify the underlying processes.

4.3.1 Temperature dependence of the coercive field

Figure 4.14 shows the coercive field for forward poling at different temperatures. It can be seen for both types of samples that the E_C values continuously decrease up to the highest achieved temperature of 520 K,

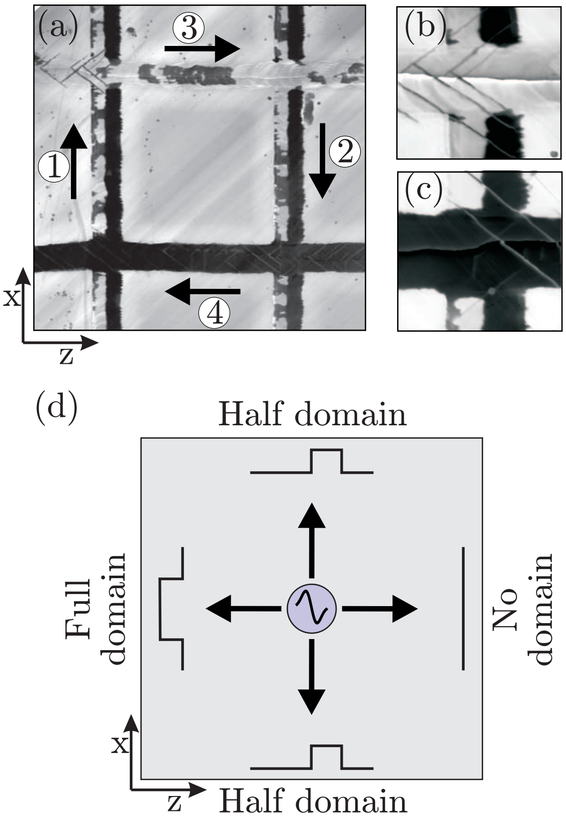

Figure 4.13: Dependence of the poling on the direction of the laser beam movement. (a – c) PFM images showing the influence of both the direction and the chronology of laser irradiation (from ① to ④) on a y-cut CLN crystal. The image sizes are $30 \times 30\,\mu\mathrm{m}^2$ (a) and $5 \times 5\,\mu\mathrm{m}^2$ (b and c). (d) shows a schematic with the laser beam at the center showing the poling behavior for different scanning directions. The arrows indicate the direction of the movement of the laser beam across the sample surface and the resulting domain pattern for the corresponding scanning direction is indicated. As in Fig. 4.12, only the half of the laser-irradiated track pointing towards the $+z$ direction is domain-inverted for scanning perpendicular to the z-axis.

at which E_C shows less than 50% of its room temperature value for both materials. No saturation of the E_C decrease is observed.

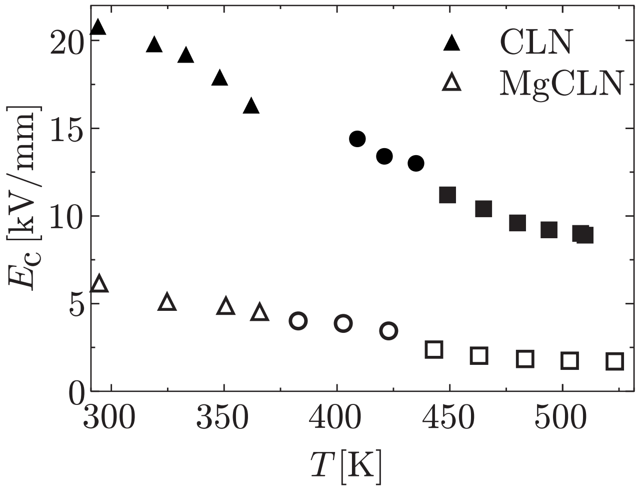

Figure 4.14: Temperature dependence of the coercive field strength E_C for undoped (CLN) and magnesium-doped crystals (MgCLN). The different shape of the symbols indicates the different liquid electrodes used. *Triangles*: saturated, aqueous calcium dichloride solution; *Circles*: cinnamyl alcohol; *Squares*: binary salt mixture of potassium nitrate and lithium nitrate.

The different types of liquid electrodes introduce a small systematic shift of the data points, but the overall trend, a decrease of E_C with increasing temperature, is still distinct.

The amount of redistributed compensation charges for different poling temperatures was determined from integrating the corresponding poling current and found to be constant within the experimental accuracy being about ±5%. This indicates that, in the studied temperature range, the spontaneous polarization is constant within a 10% margin.

To investigate whether the internal field, supposed to be generated by frustrated defect clusters (see Sec. 2.1.3), is affected by heating and UV illumination, poling cycles were performed at room temperature, and the hysteresis loops were recorded. In Fig. 4.15, E_{int} can be clearly seen as a shift of the hysteresis loop along the abscissa. Poling of the crystals at 470 K followed by cooling down to room temperature with the field still applied to the crystals results in a permanent inversion of the internal field for $LiNbO_3$ (see Fig. 4.15). The internal field for CLN is measured to be 2.7 kV/mm and can be reversed by 87%. For MgCLN, the internal field is 0.6 kV/mm and can be reversed by 66% (see Fig. 4.15).

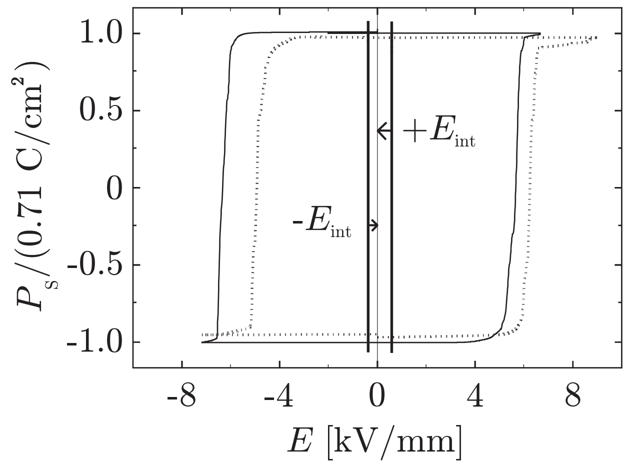

Figure 4.15: Spontaneous polarization P_S vs. the externally applied electric field E. An asymmetry of the hysteresis loop for as-grown MgCLN (dotted line) and for the same crystal at room temperature after poling one time at a temperature of 470 K (solid line) is obvious (E_{int}: so-called internal electrical field).

Furthermore, the effect of homogeneous UV illumination with light of a wavelength of 351 nm on the internal field is investigated. The $LiNbO_3$ crystals were poled one time with UV illumination and then, without illumination, a hysteresis loop was recorded. No effect on the internal field was observed after UV illumination.

4.3.2 Coercive field reduction by UV illumination at elevated temperatures

The dependence of the coercive field strength of MgCLN on the intensity of the UV illumination at room temperature is shown in Fig. 4.16. The reduction of E_C happens as soon as the sample is illuminated, is not accumulative and completely reversible, i.e., E_C jumps back to the pre-exposure value, as soon as illumination is stopped. Heating of the MgCLN crystal by the UV light at these intensities can be neglected, considering the low absorption of the crystal at this wavelength [30]. For intensities above $400\,mW/cm^2$, E_C saturates at 40% of its initial value of 6.5 kV/mm. For CLN, the coercive field strength is not influenced by illumination with weakly absorbed UV light [30].

To investigate, whether the effects of E_C reduction by heat and E_C reduction by UV light can be superimposed, an MgCLN crystal is heated up to 500 K and then kept at this temperature, while E_C is measured for

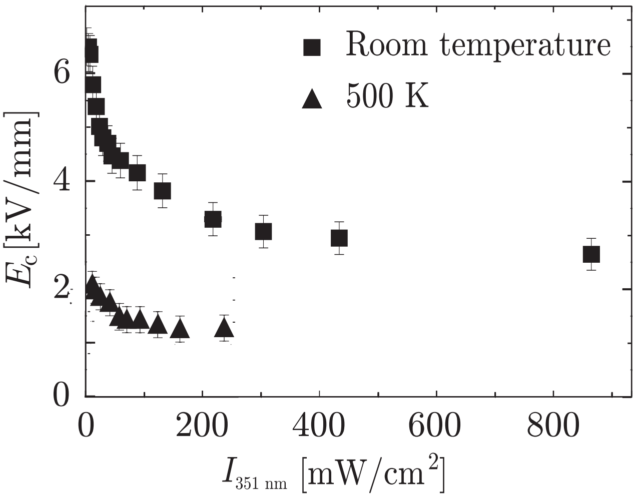

Figure 4.16: Dependence of the coercive field strength E_C of magnesium-doped crystals (MgCLN) on the intensity I of homogenous illumination with UV light (351 nm) at room temperature (squares) and at 500 K (triangles).

illumination with different UV intensities (see Fig. 4.16). Again, E_C decreases with increasing UV intensity, clearly below the saturation value for MgCLN obtained at room temperature (see Fig. 4.16) and saturates at 1.3 kV/mm.

4.3.3 Coercive field reduction of chemically reduced lithium niobate

Since as-grown CLN shows no E_C reduction for illumination with weakly absorbed UV light [30], we investigate whether this can be changed by the vacuum annealing that induces stable bipolarons (Sec. 3.1). The E_C of the vacuum-annealed CLN crystal without UV illumination is 20.5 kV/mm, which is identical to the value of as-grown CLN. But, contrary to the as-grown CLN, E_C of the reduced CLN decreases with increasing UV intensity and saturates at a value around 10 kV/mm (see Fig. 4.17). As in the case of MgCLN, the coercive field reduction is reversible, transient and does not depend on the illumination time.

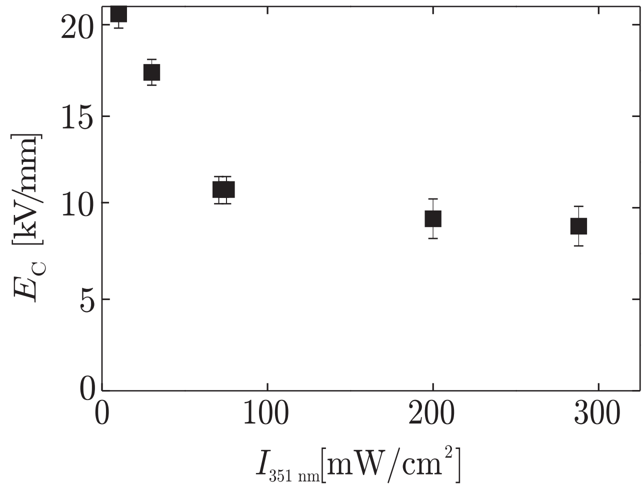

Figure 4.17: Dependence of the coercive field strength E_C for chemically reduced CLN on the intensity $I_{351\,\mathrm{nm}}$ of homogeneous illumination with UV light (351 nm).

Chapter 5

Discussion

5.1 Domain patterning with structured electrodes

In this work, an approach is taken to overcome the limitations of standard EFP, i.e. to generate bulk domain patterns in Mg-doped $LiNbO_3$ with short period lengths by utilizing the effects of heat and UV light on the domain wall kinetics.

For MgCLN the approach to spatially modulate the electric field and the coercive field by a structured photoresist did not yield the desired bulk-domain structures with short period lengths. As Fig. 4.1 indicates, a domain pattern is generated on the $+z$ face that reflects the periodicity of the photoresist structure (period length: 10 µm). Even though, on the $+z$ face the pattern is ”overpoled”, i.e., the duty cycle (width of inverted domain/ period length) exceeds 0.5, no domain patterning on the $-z$ face is observed. The duty cycle of the liquid electrode pattern of 0.1 (electrode width/period length), generated by the structured photoresist, already takes into account the sideways growth of domains in ferroelectric oxide crystals [82, 105]. The electrode width of 1 µm for the period length of 10 µm already is at the limit of resolution for this lithography method, but parameters that still could be optimized for bulk-domain patterning would be the shape, length and number of the HV pulses that are applied to the crystal (see Fig. 4.3).

For MgSLN the results for the same experimental approach are significantly better than those for MgCLN. As indicated in Fig. 4.4 the electrode pattern (period length 10 µm) is mostly translated into domain a pattern with a duty cycle around 0.5 and the domains mainly do not merge as they grow from the $+z$ face to the $-z$ face [106]. The current detected during pulse poling indicates a non-ohmic behavior and therefore can be related to the redistribution of compensation charges (see Fig. 4.3). The fact that the poling current only flows in the time interval between 240 ms and 280 ms, at the peak-voltage and the following plateau, indicates that the appropriate amplitude of the HV pulse (3.1 kV/mm) has been found for domain patterning [107, 108]. The chosen value of 40 mW/cm^2 for illumination of the crystal with UV light of 334 nm decreases the coercive field strength to 50% (see Fig. 4.2) in the uncoated areas that are contacted by the liquid electrodes. In the coated areas, 48% of the UV light is absorbed by the photoresist and we expect a coercive field reduction to 54% of its original value. Therefore, even underneath the coated area E_C is significantly reduced and the spatial modulation of the E_C reduction is 4% (0.26 kV/mm). This modulation of the field may look small at first glance. However, since domain inversion is a threshold process, this modulation is fully sufficient for domain structuring. Using lower UV intensities would increase the modulation of E_C (see Fig. 4.2), but then discontinuous and thus uncontrolled domain growth occurs. At the same time, the high electrical resistance of the photoresist ensures a structured electric field.

Smaller period lengths with a domain duty cycle of 0.5 are desired, but the thickness of the photoresist, which should be sufficient to provide reasonable UV light absorption, limits the smallest structures to 1 µm for a 1.5-µm-thick photoresist pattern. Optimization of the UV intensity to values less than 40 mW/cm^2 could increase the quality of the domain pattern and lead to periodically poled Mg-doped $LiNbO_3$ with smaller period lengths.

In contrast to MgCLN, the spatial modulation of E_C by a UV light pattern in MgSLN significantly improves the resulting bulk domain pattern, even though both materials are susceptible to reversible E_C reduction up to 50% by weakly absorbed UV light. One possible explanation for this difference relates to the frustrated defect structures (see Sec. 2.1.3), which also appear with a slightly different structure in MgCLN that pin domain walls [29]. These defect clusters that hinder the translation of the electrode pattern to a bulk domain pattern for short period lengths are not prominent in MgSLN. As described in detail later in Sec. 5.3, the UV light can only provide screening charge carriers for the frustrated defects, but not reverse them like EFP can at elevated temperatures.

5.2 Domain patterning by UV irradiation

Domain patterning by poling inhibition is a multiple-step process consisting of the UV irradiation of the crystal and the subsequent EFP. To understand the underlying mechanisms, it is crucial to understand the generation process and the character of the latent state and how the latent state is translated into a domain pattern. However, for the direct writing on the non-polar faces, the poling mechanism has to be linked directly to the irradiation with focused UV light.

5.2.1 The origin of the latent state

To begin with, it is considered whether the latent state can be associated with the space-charge fields recorded during the UV irradiation, a straightforward explanation of PI that was initially suggested [78]. The experimental results, however, allow the exclusion of this hypothesis (see Sec. 4.2.2): During the annealing at 520 K, the hydrogen ions become mobile, and space-charge fields would be compensated within a few minutes via the ionic conductivity [109]. A similar fast compensation would occur during the illumination with weakly absorbed UV light which, as is known, causes a strong photo-conductivity in MgCLN [30]. Since poling inhibition is insensitive to these two intermediate treatments [110], it cannot be linked to space-charge fields.

Therefore an explanation of the experimental data on PI (Sec. 4.2) by changes of the lithium concentration is discussed. First of all, it should be theoretically estimated how irradiation with strongly absorbed focussed laser light changes the Li concentration immediately below the irradiated surface.

5.2.2 Modeling of lithium thermodiffusion

Congruent $LiNbO_3$ crystals possess a large lithium deficiency and Li vacancies must be considered as the primary migrating species. These vacancies are charged and their concentration, N, can roughly be estimated as $\sim 10^{20}\,\mathrm{cm}^{-3}$ in the initial state [111]. The sign and the value of the concentration change δN in the latent state are discussed here in detail. With δN known, the change of the absolute Li concentration can obviously be evaluated as $\delta N_{\mathrm{Li}} = -\delta N$. Since the Li ions do not occupy interstitial sites, the temporal change of the δN_{Li} can be linked to the temporal change of δN as two counter-propagating fluxes.

Determination of the concentration changes separates into two problems: First, the temperature profile $T(\mathbf{r}, t)$ during UV exposure needs to be known. This problem has been treated theoretically by Muir et al. [112], where the temperature distribution below the UV-irradiated surface was solved analytically and just the last integration step had to be solved numerically. The main outcome is that the changes of T are well-localized (within roughly the beam radius r_0) and follow adiabatically the UV intensity distribution for the scanning velocity v of 100 µm/s. Hence, the characteristic time of the temperature changes at a certain point of the laser track is $t_0 = 2r_0/v$; it can be estimated as $t_0 \sim 5 \times 10^{-2}$ s for the standard UV irradiation parameters to generate the LS (see Sec. 3.4.2). As for the peak temperature T_*, it is close to the melting point, about 1523 K [13].

The second aspect to be treated, would be the thermo-activated spatial migration of Li vacancies. The necessary large changes of N are possible only under the condition of almost full compensation – otherwise huge electrostatic forces would quickly prevent the spatial changes of N. Free charge carriers (electrons and/or holes) UV-excited via band-to-band transitions are best suited for the charge compensation. These are single-photon transitions as the energy of a UV quantum at 275 nm, $\hbar\omega \simeq 4.3$ eV, exceeds the band gap of lithium niobate ($\simeq 3.7$ eV). We assert here that the UV-induced free-carrier conductivity exceeds the thermo-activated conductivity caused by Li ions, i.e., migration of lithium vacancies is the bottleneck for the spatial changes of N.

To verify this, one has to take into account that the combination $\alpha I/\hbar\omega$ is the number of light quanta absorbed in a unit volume during a unit time; it gives the rate of excitation of free charge carriers assuming a quantum yield of 100%. By multiplying this rate by the effective lifetime τ (most probably, the electron lifetime), the free-carrier concentration n is obtained. Multiplying n by the effective free-carrier mobility μ and the elementary charge e, gives the free-carrier conductivity as $\sigma_{\text{fc}} = e(\alpha I/\hbar\omega)\mu\tau$. Using the Einstein relation [113] between the diffusion coefficient of Li vacancies D_{Li} and their mobility, the conductivity of Li ions is estimated as $\sigma_{\text{Li}} = e^2 N D_{\text{Li}}/k_B T_*$, where $D_{\text{Li}} = D_0 \exp(-E_{\text{a}}/k_B T_*)$, k_B is the Boltzmann constant, and E_{a} is the activation energy for Li vacancies. Therefore, the condition of domination of the free-carrier conductivity is

$$\frac{\alpha I}{\hbar\omega}\,\mu\tau \gg \frac{eN}{k_B T_*}\,D_{\text{Li}}(T_*)\ . \tag{5.1}$$

Despite a rather large spread of the literature data on the pre-exponent D_0, the activation energy E_{a}, and the $\mu\tau$ product [101, 114], one can make an estimate whether this restriction is fulfilled under the current experimental conditions. Using $D_0 = 0.1$ cm^{2}s^{-1} and $E_\mathrm{a} = 1.2$ eV as reasonable values for our experimental conditions [101] and $\mu\tau = 5 \times 10^{-10}$ cm^{2}V^{-1} for temperatures close to T_C [115], one obtains that the left side of Eq. 5.1 is two orders of magnitude larger than the right side and therefore the relation is safely fulfilled.

It is important that the Maxwell (space-charge field) relaxation time $t_M = \epsilon\epsilon_0/\sigma_\mathrm{fc}$, where $\epsilon\epsilon_0$ is the static permittivity, is expected to be much shorter than the heating time t_0. This means that the pyroelectric field $P_\mathrm{S}/\epsilon\epsilon_0$, where P_S is the room-temperature spontaneous polarization of lithium niobate, is strongly compensated by the free charge carriers. This compensation would be complete for a steady-state heating, and it is almost complete for $t_M \ll t_0$. As a result, the value of the space-charge field generated by the pyro-electric effect can be estimated as:

$$|E_\mathrm{sc}| \lesssim (t_M/t_0)\, P_\mathrm{s}/\epsilon\epsilon_0 \ll P_\mathrm{s}/\epsilon\epsilon_0\,. \tag{5.2}$$

To judge whether Li-enrichment or Li-depletion occurs in the heated volume, the sign and the value of the concentration changes have to be considered. The actual situation with these issues is unusual in the sense that the spatial changes of $N(\mathbf{r})$ are driven by ∇T instead of ∇N. This means that the most familiar Fick's law is not applicable, and there is need to link the flux of lithium vacancies to the strong temperature gradients. However, this situation is not exceptional for the transport phenomena, where the temperature gradients are regarded, together with the concentration and other gradients, as a common driving force for the fluxes of different physical quantities [116].

The distinctive feature of ion transport in solids is its hopping character – ions must overcome rather high energy barriers in order to hop to allowed neighboring positions. The most important features of this transport can be reliably understood and described within elementary hopping models [117]. This case of thermodiffusion is not exceptional.

In the standard one-dimensional hopping model, the probability of a hopping event is proportional to the exponential factor $\exp(-E_\mathrm{a}/k_BT)$, see also Fig. 5.1. The only possible hopping processes here are hops of the left and right Li ions to the empty central position, which means hops of the vacancy to the left and right, respectively. Since the temperature T_1 at the left barrier is larger than the temperature T_2 at the right one, the thermally activated probability for the left ion to hop is larger than that for the right ion. Correspondingly, the vacancies migrate on average to the left. So, the overall flux of Li vacancies is aligned parallel to the temperature gradient, whereas the flux of Li ions is aligned anti-parallel to ∇T. This leads to *depletion of lithium* in the illuminated area. It is easy to see that the situation would be reversed for migrating interstitial ions. It is important to note that this diffusion model is only valid, if the concentration of the Li ions is large in comparison to the concentration of the Li vacancies, which still holds for CLN and MgCLN.

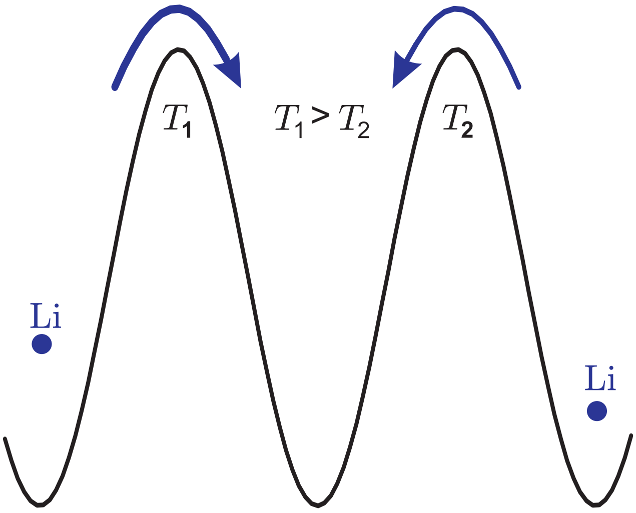

Figure 5.1: Illustration of the hopping migration of Li ions driven by a temperature gradient. The central empty position corresponds to the vacancy, so that the left/right ions can only hop to the right/left, respectively.

The flux of Li ions, J_{Li}, within the hopping model can be evaluated as

$$J_{\mathrm{Li}} = -N\nabla D_{\mathrm{Li}}. \tag{5.3}$$

Taylor expansion of the exponential factor of the function for D_{Li} to the second term yields:

$$J_{\mathrm{Li}} \propto -\nabla T. \tag{5.4}$$

Generalization from the one-dimensional to the three-dimensional case would change only secondary details. The change of the absolute Li concentration δN_{Li} can now be estimated from the continuity equation

$$\frac{\partial \delta N_{\mathrm{Li}}}{\partial t} + \nabla J_{\mathrm{Li}} = 0\,. \tag{5.5}$$

Replacing the derivatives $\partial/\partial t$ and $\partial/\partial r$ by the characteristic values t_0^{-1} and the beam radius $(r_0)^{-1}$, the estimate

$$\frac{|\delta N_{\mathrm{Li}}|}{N} \sim \frac{4\, t_0\, D_{\mathrm{Li}}}{r_0^2} \frac{E_{\mathrm{a}}}{k_B T_*} \tag{5.6}$$

is obtained. By setting $E_{\mathrm{a}} = 1.4\,\mathrm{eV}$ [101], $D_0 = 0.1\,\mathrm{cm}^2/\mathrm{s}$ [101], $r_0 = (2.5 \pm 0.75)\ \mu\mathrm{m}$, we obtain $\delta N_{\mathrm{Li}}/N \sim 1$. The accuracy of this rough estimate is probably within less than two orders of magnitude, since values that have a strong influence on the result, e.g., E_{a} and T_*, are not exactly known. Anyhow, it shows that the depletion of the Li concentration during the UV exposure is very strong. By going into more detail, one can make sure that the UV-induced reduction of $N_{\mathrm{Li}}(r)$ at the beam center is accompanied by a noticeable increase at the beam periphery. This comes just from the fact that the lithium ions pushed out of the central region cannot go far away from it. Note that evaporation of lithium through the surface is neglected in this model as this potentially competitive process is characterized by a considerably larger activation energy [101, 118].

The pyroelectrically driven space-charge field $E_{\mathrm{sc}}(t)$, mostly compensated by photo-excited electrons, is positive during the cooling stage and nonzero after this stage and therefore, additionally provides a shift of the depletion area to the crystal depth and non-equivalence of the $+z$ and $-z$ faces of the crystal. The value of the shift is controlled by the $\mu\tau$ product which cannot be reliably estimated at $T \approx T_*$. Ying et al. [100] observed buried PI domain structures in CLN, indicating that the absolute minimum of the Li concentration is several µm below the $+z$ face, which is a strong indicator for an additional shift of the Li ions by the pyroelectric field.

In this section, it was intended to link the increase of the coercive field in the latent state (see Sec. 4.2.3) to a UV-induced change of the lithium concentration. A claim for a perfect agreement between theoretical results and experimental observations is unrealistic because of the complexity of the problem and the uncertainty in the values of the main material parameters, especially at temperatures close to T_{C}. The analysis and deductions are therefore a qualitative description of the PI phenomenon with rough estimates of the crucial parameters.

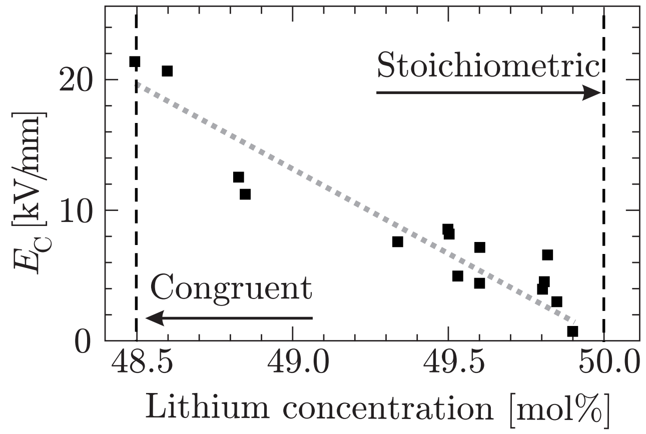

Figure 5.2: Dependence of the coercive field E_c on the degree of stoichiometry of lithium niobate crystals (lithium concentration: $Li/(Li + Nb)$). The data points are taken from the literature [49–52], and the dashed line is a linear fit. Note that due to a different manufacturer of the SLN or different determination methods of E_c, values for SLN differ from our measured value of 5 kV/mm

5.2.3 Discussion of the experimental results in the framework of the model

The redistribution of Li ions is considered as a possible mechanism and the experimental results are discussed in the context of the Li-thermodiffusion model (see Sec. 5.2.2). According to the estimates, the changes of Li concentration can be strong after primary UV irradiation.

The absence of any effect of the mentioned two of the three intermediate treatments on the latent state (see Tab. 4.1) now looks understandable – these treatments do not make lithium ions mobile. However, heating to 670 K is sufficient to activate diffusion of Li vacancies and to allow the Li ion concentration to become more evenly distributed during the one-hour annealing procedure.

The presence of a pronounced depletion of lithium in the latent state is furthermore sustained by the fact that the UV-irradiated tracks, scanned with similar scanning parameters, are found to act as channel waveguides [119]. From the studies of the mode profiles it is possible to evaluate the refractive index changes [120]. The latter can be directly linked to the Li depletion [121] which can be estimated as 4 mol%. This number is in reasonable agreement with the results of Sec. 5.2.2.

It is now relevant to deduce the impact of the change of stoichiometry on the coercive field. This can be assessed for CLN from Fig 5.2 that is based on literature data [49–52]. It shows that E_C strongly increases at approximately 10 kV/mm per 1 mol% decreasing relative Li concentration below the stoichiometric composition, in the case of undoped $LiNbO_3$. For Mg-doped crystals, the values of E_C for MgCLN (6.5 kV/mm) and MgSLN (3 kV/mm) indicate the same trend. As a consequence, the UV-induced depletion of lithium inside the heated volume can lead to a strong increase in E_C and therefore, to poling inhibition.

The data on local poling by a PFM tip, shown in Fig. 4.7, gives further insight into the physical mechanism responsible for PI and supports the lithium thermodiffusion model, as well. For the low intensity case ($I_{UV} = 1 \times 10^5$ W/cm^2) the resulting domain-inverted area is actually broader than the area that has been scanned by the PFM, which lies in-between the two horizontal dashed lines shown in Fig. 4.7(b). It is caused by sideways spreading of domains during the growth; this effect is well known for EFP and is even more pronounced when applying the field through a sharp tip, since the field distribution is strongly nonuniform. This effect is even stronger around the latent state, indicating smoother domain wall propagation, which is known for annealed congruent crystals, since domain wall pinning frustrated defect clusters are reduced [29]. Furthermore, there is a slight deterioration of the poling quality within the UV-irradiated area, which manifests itself in numerous bright spots, best seen in Fig. 4.7(b). This can be attributed to statistically distributed PI nano-domains that emerge in regions where E_c is slightly increased in comparison to the untreated crystal.

For the case of irradiation with higher UV laser power ($I_{UV} = 2 \times 10^5$ W/cm^2), the poling behavior changes dramatically as shown in Fig. 4.7(c). The PFM-poled stripe is interrupted, when crossing the laser track area and poling is inhibited here. Note that the transition from the poled to the unpoled region is not abrupt, but occurs via an intermediate region with partial poling, which can be seen in Fig. 4.7(d). This state is similar to the state in Fig. 4.7b, which indicates again a slight increase in E_C. The PFM-poled horizontal stripe experiences extensive broadening, when approaching the LS. Evidently, strong sideways spreading of the domains in facilitated in this region. This points to a local *decrease* of E_C, which agrees with statement of the Li-diffusion model (5.2.2) that predicts an $Li - enrichment$ adjacent to the UV-irradiated track and therefore, a stoichiometry closer to the case of SLN.

The physical mechanism behind inhibited poling for $LiNbO_3$ has been investigated, both experimentally and theoretically and both results point to thermodiffusion of Li as the driving mechanism [110]. The fact that PI could not be observed in SLN and MgSLN (see Fig. 4.2.1) supports this conjecture: Near-stoichiometric $LiNbO_3$ contains insufficient Li-vacancies to obtain an efficient redistribution of Li-ions, so the increase of E_C inside the UV-irradiated track is not sufficient to obtain PI.

5.2.4 Bulk domain patterning by poling inhibition

For two consecutive EFP steps after UV-irradiation, the latent state is translated into a bulk domain pattern for MgCLN (see Sec. 4.2.4), whereas for CLN, so far, only surface domains with a depth of less than 2 μm have been observed. The exact mechanism that enables the surface domains to translate into a bulk domain pattern without merging has not been clarified, yet. The indicator that coincides with the bulk-domain generation, the abnormally high amount of charge transfer during the second EFP step, can have various origins: It is known that the electrical resistance in $LiNbO_3$ crystals with domain patterns with period lengths in the regime of tenths of μm decreases by two orders of magnitude [122]. Domain walls are proposed as a possible reason for this effect, which matches the observation that the decreased resistance is only observed during the second EFP step, where the bulk domain walls are actually generated. Another possible reason might be that when a high voltage with the right polarity is applied to the UV-irradiated $+z$ face, a chemical reaction at the surface occurs that releases ions into the liquid electrode and generates a current signal.

5.2.5 Domain patterning for whispering gallery mode resonators

The application of the bulk domain patterning by PI in WGRs is promising, since the versatility that PI has is used here: the fabrication process permits the LS to be written on a crystal which has already been fixed on a metal rod. This metal rod is mounted as the axis of rotation in both, the rotation setup for the UV laser irradiation and during the diamond turning and polishing.

This yields a good alignment between the center of the radial domain structure and the center of the toroid, leading to high efficiency for the non-linear process [103]. This fabrication method would be hard to realize for conventional domain patterning with structured electrodes and HV pulses, because poling with HV pulses leads to short pulses of mechanical stress via the piezoelectric effect that usually breaks samples that are fixed to other structures by glue. The bulk domain pattern has a sufficient depth that the WGR mode, simulated in Fig. 4.10, overlaps with a periodically poled domain structure (see Fig. 4.9).

However, a relatively high threshold for the optical parametric oscillation is expected, which is due to the duty cycle at the fringe of the WGR of around 0.2. To achieve a duty cycle around 0.5 a UV light power of around 150 mW would be needed to generate a focal spot with a width of 15 µm that would still overcome the intensity threshold for PI.

From Fig. 4.9 it also becomes clear that, even though on the $+z$ face with essentially arbitrary angles with respect to the y-axis PI surface domains can be generated, for certain angles the bulk domain pattern has gaps, where the surface domains have not grown into the crystal bulk. It can be seen that the projection of the radial structure on a secant plane shows two gaps that are equidistant to the symmetry axis of the radial LS pattern (Fig. 4.9). This indicates that under an angle around 30° with regard to the y-axis bulk domain growth is inhibited. It can be explained by the fact that domain walls grow parallel to the y-axis [85] and due to the hexagonal structure of $LiNbO_3$, the angle 30° represents the bisection of two y-axes, making domain wall growth along this direction most unfavorable [123].

5.2.6 Direct domain writing on the non-polar faces

The results from Sec. 4.2.6 indicate that UV irradiation of the non-polar x- and y-faces of $LiNbO_3$ can be utilized to directly write domains similar to the direct writing of domains on the polar $-z$ face [77]. Even though the irradiation parameters are similar to PI and direct writing on $-z$, a new underlying mechanism has to be discussed, since in the case of the non-polar face, the direction of P_S is always perpendicular to the incident laser beam and the resulting domain structures strongly depend on the scanning direction.

In order to understand this mechanism one can refer to experiments where crystals were subjected to temperature gradients along the z-axis, either by annealing in an oven exhibiting a non-uniform temperature profile [124], or local heating by irradiation with a strongly absorbed IR laser beam [125]. In both experiments, the direction of the spontaneous polarization was observed to follow the projection of the temperature gradient on the crystals z-axis: In the case of the annealing procedure, the $+z$ face developed at the warmer end of the crystal and for the case of local heating by irradiation by an focussed IR laser, a head-to-head domain formed with the domain wall at the maximum of the temperature profile, due to the opposing temperature gradients. Both references presume that the temperature gradient inside the crystal causes an electric field, whose origin is of thermoelectric nature and the experiments are carried out at temperatures close to T_C. Since the phase transition from the ferroelectric to the paraelectric phase happens at T_C, it can be understood that close to T_C the coercive field is below 100 V/mm [83]. Consequently, even small electric fields are sufficient to reorient the spontaneous polarization of the crystal.

This mechanism applies also to our scenario of local heating by a focussed UV laser beam as is schematically illustrated in Fig. 4.15. Due to the strong absorption of the UV laser light, the crystal is locally heated close to its melting temperature, giving rise to a temperature profile with a local maximum and therefore, a change of sign of the temperature gradient, as shown in Fig. 5.3(a). The temperature for very similar irradiation conditions was modeled by Muir et al. and it is shown that the actual width of the temperature profile slightly exceeds the width of the laser beam [112]. Using this model for the temperature distribution, an estimate is made whether the magnitude of the bi-polar field is sufficient to pole the crystal: Between the center of the laser beam and the position where the intensity has decreased to 1/e, the temperature gradient can be roughly approximated to be $\Delta T \approx 200$ K/µm. Together with the appropriate value of the thermoelectric tensor $Q_{33} = 0.8$ mV/K [125], a thermoelectric field of 160 V/mm is obtained, which is sufficient to set the direction of the spontaneous polarization at temperatures close to T_C.

Therefore, the bipolar electric field inside the heated volume [see Fig. 5.3(b)] causes domain inversion within half of the volume [see Fig. 5.3(c)] with the field polarization aligned antiparallel to P_S [126]. The width d of the resulting inverted domain depends on the strength of the bipolar electric field, and is thus expected to depend on the degree of focusing and the power of the irradiating laser beam.

All observations described in Sec. 4.2.6 are in accordance with the model depicted in Fig. 5.3. So far, laser writing perpendicular to the z-axis only has been discussed. In the framework of the proposed UV laser-induced bi-polar electric field, the results obtained on a y-cut CLN crystal and laser writing along both x- and z-directions can be explained. The observed domain pattern dependening on the scanning direction is schematically depicted in Fig. 4.13(d). The experimental result obtained by PFM imaging is shown in Fig. 4.13(a – c).

These results perfectly meet the assumption of the emergence of a bipolar electric field, caused by local heating of the crystal whereby the direction of the z-axis determines the bipolar characteristics. The poling behavior is set by the following two rules: (i) For a crystal with the $+z$ axis oriented towards the right as shown in Fig. 4.13(a), only the negative part

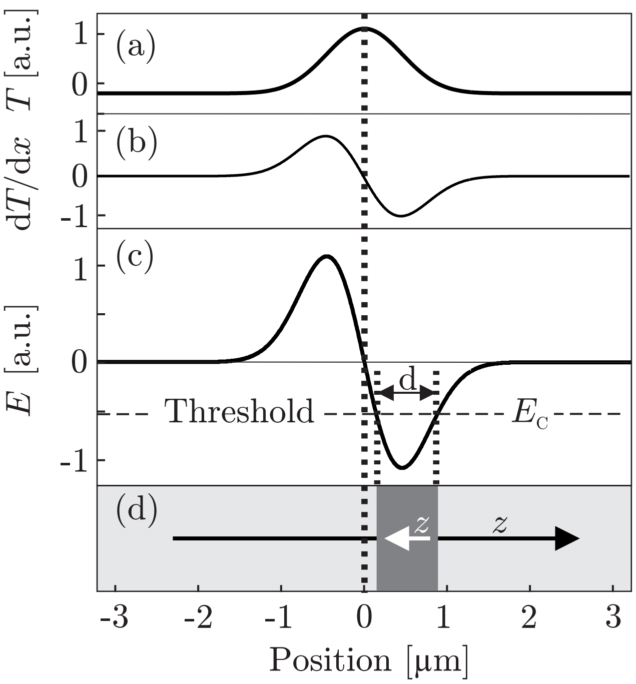

Figure 5.3: Schematic illustration of the mechanism for domain inversion of an *x*- or a *y*-cut $LiNbO_3$ crystal upon UV-laser irradiation. Due to the high absorption of the material, the crystal is locally heated close to its melting point (a) leading to opposed temperature gradients. A bi-polar thermoelectric field builds up (c), which, in a region of width *d*, exceeds the coercive field E_C and therefore, leads to domain inversion. The resulting domain pattern is shown in (d).

of the electric field will lead to domain inversion; in case of the crystal being oriented the other way round ($+z$ pointing towards the left) evidently only the positive part of the electric field will lead to domain inversion. (ii) The orientation of the polar z-axis on the laser-written track is determined by the polarity of the electric field that each spot on the laser-written track experiences at last, while the laser focus propagates. A major argument for the bi-polar field can be found in Fig. 4.13(b, c), where the junctions of a track written parallel to the x-axis with track ③ and track ④, respectively, are shown. In the case of ③ the trailing "positive" part of the bipolar field even erases the previously written "half-domain" structure, whereas in the case of ④ the trailing "negative" part of the bi-polar field domain-inverts the entire structure.

The experiments on the non-polar x- and y-faces of $LiNbO_3$ presented in Sec. 4.2.6 are a further facet of our investigations on laser-induced domain formation with a tightly focussed, strongly absorbed UV-laser beam using $LiNbO_3$ crystals. To show the *big picture*, one can put the findings of the x- and y-faces in the context of the results previously obtained on the polar faces [24], the irradiating parameters being the same in all cases as depicted in Tab. 5.2.

Crystal face	Poling method	Driving mechanism
x-face	Direct writing	Bipolar electric field
y-face	Direct writing	Bipolar electric field
$+z$ face	Poling inhibition	Li-redistribution
$-z$ face	Direct writing	UV-induced electric field

Table 5.1

Generally, it can be said that on the x- and y-faces and the $-z$ face, direct poling upon laser irradiation is observed whereas on the $+z$ face, poling inhibition, and thus domain formation only after subsequent electric field poling, is found. According to our current understanding, domain formation on all faces relies on the heat profile generated in the crystal via laser irradiation. This is supported by the fact that on all faces the depth of the generated domains is of the same order (a few microns) and domain shaping is independent of the crystallographic axes, only following the laser-written track. In the case of x- and y-faces and the $-z$ face, the alignment of the spontaneous polarization parallel to the temperature gradient is assumed to be the driving mechanism for direct domain formation, whereas in the case of poling inhibition, which is observed on the $+z$ face, lithium redistribution is found to play a crucial role.

One can now compare the different poling methods investigated in this work and the standard domain patterning methods known from literature with each other (see Tab. 5.1). For CLN z-cut crystals bulk domain patterns with short period lengths can be generated by standard EFP methods [25]. For MgCLN z-cut crystals, bulk domain patterning by EFP and structured electrodes a minimum domain width of one micron is achieved but the domain pattern has only a depth of 150 µm [26]. EFP at elevated temperatures or illumination with weakly absorbed UV light leads to deeper domain patterns at short period lengths [63, 64, 106]. Bulk domain patterns generated by PI in MgCLN have already reached minimum widths and maximum depths in the same regime but also offer the advantage that the domain patterns can be generated at arbitrary angles with regard to the y-axis 4.2.4.

For the non-polar faces, domain patterning has so far only been realized for ridge waveguide structures, which effectively is also EFP along the z-axis by structured electrodes on the sides of the ridge [127]. The direct writing by strongly absorbed UV light offers a method to generate domain patterns on planar non-polar faces [126]. This would then allow for, e.g., domain patterning on the fringe of whispering gallery mode resonators [103].

Poling method	Material	CF	DW [µm]	DD [µm]	REF
Structured electrodes	CLN	z	1.4	500	[25]
Structured electrodes	MgCLN	z	1	150	[26]
Structured electrodes	MgSLN	z	3.9	500	[128]
Structured electrodes	CLN	x/y	8.3	3.5	[127]
Structured electrodes (400 K)	MgCLN	z	15	3000	[64]
Structured electrodes and UV	MgCLN	z	7.7	500	[63]
Structured electrodes and UV	MgSLN	z	5	500	[106]
UV-direct writing (244 nm)	MgCLN/CLN	$-z$	2	-	[77]
Poling inhibition (275 nm)	MgCLN/CLN	$+z$	4	4	[100]
Poling inhibition (275 nm)	MgCLN	$+z$	5	500	Sec. 4.2.4
Direct writing (275 nm)	MgCLN/CLN	x/y	1	>2	[126]

Table 5.2: Different domain patterning methods for $LiNbO_3$. CF = crystal face; DW = minimum domain width; DD = maximum domain depth; REF = reference.

5.3 Influence of heat and UV light on the coercive field

5.3.1 Influence of heat on the coercive field

At first, the reduction of the coercive field strength for $LiNbO_3$ at elevated temperatures up to 520 K described in Sec. 4.3 is discussed. For 520 K, E_C is reduced to less than 50% of its value at room temperature.

Battle et al. proposed for lithium tantalate crystals that defect structures such as frustrated antisite defects, which strongly pin domain walls and cause the internal field, can be reoriented to normal defect clusters, since heating raises the ionic conductivity [37]. Reducing the number of frustrated defects reduces domain wall pinning. Thus, domain walls propagate more smoothly at lower field strengths, and therefore a lower coercive field is observed. In the case of CLN, Kim et al. proposed a polar defect cluster consisting of one niobium-on-lithium antisite defect, charge-compensated by four lithium vacancies [see Fig. 2.2(c,d)] that leads to E_{int} [38, 129]. For $LiNbO_3$, hydrogen and lithium ions are the most mobile ions, due to their small activation energy [101]. As soon as lithium ions become mobile enough they can reorient the frustrated antisite-defects in CLN and therefore domain wall pinning is reduced.

The inversion of the internal field through a combination of poling and annealing has already been reported for CLN by Gopalan et al. [130] and for MgCLN by Yao et al. [131]. It is straightforward to propose that for the case of MgCLN, a polar defect cluster is formed by a magnesium ion on a lithium site paired with a lithium vacancy for charge compensation. If the defect complex is aligned along the c-axis (see Fig. 5.4), it leads to the internal field and, in its frustrated state, to strong domain wall pinning. This argument is supported by the fact that for both materials E_{int} can be reversed easily at temperatures, at which the lithium ions are mobile.

Therefore, it is not the macroscopic increase of the ionic conductivity, but in particular the increased mobility of the lithium ions that allows modification of polar defect structures on the microscopic scale and leads to the reduction of E_C in LN at elevated temperatures.

It is worth noting that the value of the spontaneous polarization is almost constant in the investigated temperature regime: From the pyroelectric coefficient we expect a reduction of E_C of 2.5% for heating from room temperature to 520 K [132]. This is indeed smaller than the 10% experimental accuracy for the measurement of P_S.

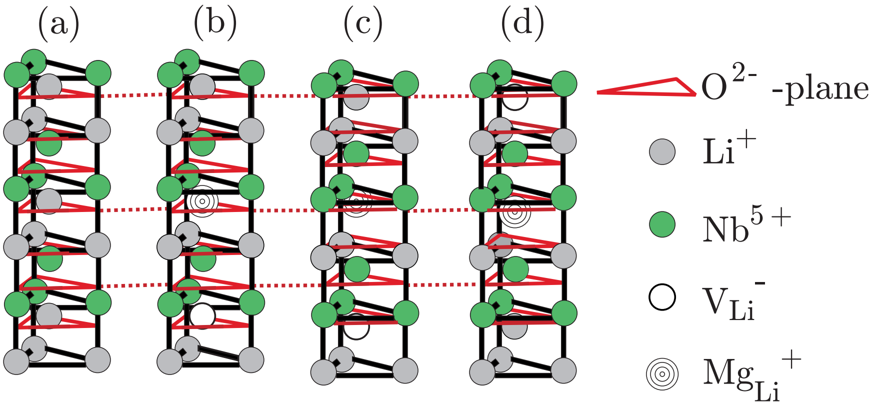

Figure 5.4: Schematic illustration of a possible defect complex involving a magnesium-on-lithium antisite defect ($Mg_{Li}{}^+$) and lithium vacancy (V_{Li}^-) in MgCLN [133] proposed analogous to the antisite defect introduced by Kim et al. [38]: (A) stoichiometric crystal without defects. (B) A dipole complex with its dipole moment oriented parallel to the c-axis. (C) The dipole complex from B after domain inversion becomes a frustrated defect with antiparallel orientation of the dipole moment in regard to the *c*-axis. (D) At elevated temperatures the lithium vacancy moves and the dipole complex aligns itself parallel to the *c*-axis again.

5.3.2 Influence of UV light on the coercive field

In the case of coercive field reduction by weakly absorbed UV light in $LiNbO_3$, it is not thermally mobilized ions but photo-excited electrons that play a crucial role. At a wavelength of 351 nm the photon energy of 3.5 eV is sufficient to excite electrons from the tail of the valence band to the conduction band. It is known that MgCLN and vacuum-annealed CLN show a larger photoconductivity than as-grown CLN [21, 134, 135]. The photo-excited electrons screen the antisite defects and therefore enable smoother domain wall propagation and lower E_C values in MgCLN and vacuum-annealed CLN but not in as-grown CLN. It is evident that the UV light does not lead to any structural change of the antisite defects, as elevated temperatures do, since no persistent change of E_{int} is observed.

It is worth noting that without UV illumination the value of E_C for the vacuum-annealed CLN is identical to the value for as-grown CLN, which indicates that the vacuum annealing itself does not lead to any effect on E_C.

Also the experimental results for simultaneous heating and UV illumination (see Fig. 4.16) can be explained with the two different E_C reduction mechanisms. First, heat helps to reduce the number of frustrated defects in MgCLN, and second, the weakly absorbed UV light photo-excites electrons that screen defects in general [133]. Based on these two different mechanisms it becomes clear that for MgCLN both effects add up and lead to an even higher reduction, so that E_C lies in the regime of SLN, since the defects have no strong impact on the poling behavior anymore.

Transient effects that lead to coercive field reduction in doped and undoped congruent lithium niobate have been investigated. The crucial mechanism, supporting domain inversion at a lower field strength, is the reduction of domain wall pinning. It is proposed that in the case of elevated temperatures this is attributed to mobilization of lithium ions, which then can restructure defects, while in the case of homogeneous UV illumination photo-excited electrons screen charged pinning defects.

5.4 Outlook

The results presented in this thesis have shown that ferroelectric domain patterns can be generated on all crystal faces by strongly absorbed UV light. Tailored domain patterning, especially in Mg-doped $LiNbO_3$ crystals, which do not exhibit optical damage, allows for a wealth of applications in non-linear optics. The principle of poling inhibition, i.e., local modulation of the coercive field due to local heating, could be further explored. The domains generated by PI have a depth of at least several microns, which would be suitable for application in optical waveguides. Focusing of the UV light to spot sizes close to the diffraction limit can yield domain patterns with period lengths in the sub-µm-range that could for instance be used for mirrorless optical parametric oscillators. The generation of bulk domains by PI offers many applications in non-linear optics, e.g., for second harmonic generation in WGRs, but the domain kinetics involved in the conversion process of the PI surface domains to bulk domains have still to be understood.

The smallest period lengths could be generated by direct writing on the non-polar faces, since the domains generated by scanning the laser beam perpendicularly to the z-axis yield domains that have only approximately half the width of the laser beam focus. Therefore, even domain widths below the diffraction limit of the writing beam could be realized. The fact that UV laser light can be used to generate domain patterns of arbitrary shape on the crystal surface has already been combined with the different etching behavior of the crystal faces to generate tailored topography patterns that can act as microresonators and ridge waveguide [19, 136]. Therefore, many tools for generating integrated optics on $LiNbO_3$ are provided by this method.

The results obtained on coercive field reduction by heat and weakly absorbed UV light give some further insight into the domain inversion process. Especially for MgCLN, the material that is most interesting for application in non-linear optics, due to its relatively low cost and the suppression of the optical damage, these two mechanisms to lower the coercive field strength have been investigated. To obtain further understanding of the influence of these external parameters on the domain inversion, confocal Raman spectroscopy could give additional information about the defect structures.

a bulk domain pattern with short period length and good duty cycle in a 500-µm-thick Mg-doped near-stoichiometric crystal could be obtained.

In contrast to the coercive field lowering mechanisms described above, focussed irradiation of $LiNbO_3$ with strongly absorbed UV light can lead to a local increase of the coercive field. UV light of 275 nm wavelength is strongly absorbed and a volume with a depth of only a few micrometers and with the size of the beam focus below the crystal surface is efficiently heated.

It depends on the irradiated face of the crystal whether the heat profile, induced by irradiation with a focussed UV laser, either leads to direct domain formation or to poling inhibition. On the $+z$ face, no direct writing of domains is observed but after an odd number of electric field poling steps inhibition of domain reversal in the UV-irradiated area is observed. This poling inhibition is investigated in detail by piezoresponse force microscopy and theoretical modeling of charge carrier migration under local exposure of strongly absorbed light. The results obtained point to the following mechanism of the poling inhibition phenomenon: strong local heating leads to a local reduction, via thermodiffusion of Li vacancies, in the Li concentration. Therefore, a strong local increase of the coercive field inside the UV-irradiated track is obtained. Together with the effect of direct writing on the $-z$ face, investigated in previous works, one can pattern domains on both z faces.

For the non-polar faces, i.e., the x- and y-faces, the laser-induced heat profile leads to the build-up of a bi-polar electric field. The projection of this field on the crystal z-axis orients the spontaneous polarization towards the temperature maximum, leading to head-to head domain structures. The bi-polar electric field along the z-axis on the non-polar faces, causes that the scanning direction determines the final shape of the domain structure. It is now the possible to generate domain patterns on all crystal faces, which is allowing for a wealth of new possibilities for applications, e.g. non-linear optics in whispering gallery mode resonators and photonic crystals.

Bibliography

[1] J. W. Goethe *Faust: Der Tragödie erster Teil*. Verse 1852, Reclam, Ditzingen, 1996.

[2] T. H. Maiman, „Stimulated optical radiation in ruby", *Nature* **187**, 493 (1960).

[3] K. R. Lang, F. S. Barnes, J. C. Daniel, and J. C. Maisel, „Lasers as tools for embryology + cytology", *Nature* **201**, 675 (1964).

[4] N. M. Saks and C. A. Roth, „Ruby laser as a microsurgical instrument", *Science* **141**, 46 (1963).

[5] J. F. Ready, „Development of plume of material vaporized by giant-pulse laser", *Appl. Phys. Lett.* **3**, 11 (1963).

[6] J. Lee, Y. Mun, S. Do, Y. Ko, D. Kong, B. Choi, J. Ming, C. Hong, and D. Jeon, „Laser tv for home theater", *Proc. SPIE* **4657**, (2002).

[7] J. M. Phillips, M. E. Coltrin, M. H. Crawford, A. J. Fischer, M. R. Krames, R. Mueller-Mach, G. O. Mueller, Y. Ohno, L. E. S. Rohwer, J. A. Simmons, and J. Y. Tsao, „Research challenges to ultra-efficient inorganic solid-state lighting", *Laser Photon. Rev.* **1**, 307 (2007).

[8] J. A. Giordmaine and R. C. Miller, „Tunable coherent parametric oscillation in linbo3 at optical frequencies", *Phys. Rev. Lett.* **14**, 973 (1965).

[9] P. Franken, A. Hill, C. Peters, and G. Weinreich, „Generation of optical harmonics", *Phys. Rev. Lett.* **7**, 118 (1961).

[10] L. E. Myers, R. C. Eckardt, M. M. Fejer, R. L. Byer, W. R. Bosenberg, and J. W. Pierce, „Quasi-phase-matched optical parametric oscillators in bulk periodically poled $LiNbO_3$“, *J. Opt. Soc. Am. B* **12**, 2102 (1995).

[11] R. G. Batchko, M. M. Fejer, R. L. Byer, D. Woll, R. Wallenstein, V. Y. Shur, and L. Erman, „Continuous-wave quasi-phase-matched generation of 60 mw at 465 nm by single-pass frequency doubling of a laser diode in backswitch-poled lithium niobate“, *Opt. Lett.* **24**, 1293 (1999).

[12] R. S. Weis and T. K. Gaylord, „Lithium niobate: summary of physical-properties and crystal structure“, *Appl. Phys. A* **37**, 191 (1985).

[13] K. K. Wong *Properties of lithium niobate.* Inspec, London, UK, 2002.

[14] L. Arizmendi, „Photonic applications of lithium niobate crystals“, *Phys. Stat. Sol. A* **201**, 253 (2004).

[15] G. A. Smolensk, N. N. Krainik, N. P. Khuchua, V. V. Zhandanova, and I. E. Mylnikov, „Curie temperature of $LiNbO_3$“, *Phys. Stat. Sol.* **13**, 309 (1966).

[16] P. F. Bordui, R. G. Norwood, C. D. Bird, and G. D. Calvert, „Compositional uniformity in growth and poling of large-diameter lithium niobate crystals“, *J. Cryst. Growth* **113**, 61 (1991).

[17] G. A. Magel, M. M. Fejer, and R. L. Byer, „Quasi-phase-matched 2nd-harmonic generation of blue-light in periodically poled $LiNbO_3$“, *Appl. Phys. Lett.* **56**, 108 (1990).

[18] C. Canalias and V. Pasiskevicius, „Mirrorless optical parametric oscillator“, *Nat. Phot.* **1**, 459 (2007).

[19] Y. J. Ying, C. L. Sones, A. C. Peacock, F. Johann, E. Soergel, R. W. Eason, M. N. Zervas, and S. Mailis, „Ultra-smooth lithium niobate photonic micro-structures by surface tension reshaping“, *Opt. Express* **18**, 11508 (2010).

[20] A. Ashkin, G. D. Boyd, J. M. Dziedzic, R. Smith, A. A. Ballman, J. J. Levinstein, and K. Nassau, „Optically-induced refractive index inhomogeneities in $LiNbO_3$ and $LiTaO_3$“, *Appl. Phys. Lett.* **9**, 72 (1966).

[21] D. A. Bryan, R. Gerson, and H. E. Tomaschke, „Increased optical damage resistance in lithium niobate“, *Appl. Phys. Lett.* **44**, 847 (1984).

[22] J. Webjorn, F. Laurell, and G. Arvidsson, „Blue-light generated by frequency doubling of laser diode light in a lithium niobate channel waveguide“, *IEEE Photonic. Tech. L.* **1**, 316 (1989).

[23] V. Shur, E. Rumyantsev, R. Batchko, G. Miller, M. M. Fejer, and R. Byer, „Physical basis of the domain engineering in the bulk ferroelectrics“, *Ferroelectrics* **221**, 157 (1999).

[24] S. Mailis, „uv laser induced ferroelectric domain inversion in lithium niobate single crystals“, *J. Opt.* **12**, 095601 (2010).

[25] M. Yamada, N. Nada, M. Saitoh, and K. Watanabe, „1st-order quasi-phase matched $LiNbO_3$ waveguide periodically poled by applying an external field for efficient blue 2nd-harmonic generation“, *Appl. Phys. Lett.* **62**, 435 (1993).

[26] K. Mizuuchi, A. Morikawa, T. Sugita, and K. Yamamoto, „Generation of 360-nm ultraviolet light in first-order periodically poled bulk $MgO{:}LiNbO_3$“, *Optics Letters* 935 (2002).

[27] K.-H. Hellwege *Landolt Börnstein - Numerical data and funtional relations in science and technology*, **III/16**. Springer Verlag, 1981.

[28] M. Lines and A. Glass *Principles and Applications of Ferroelectrics and Related Materials*. Oxford University Press, 2001.

[29] V. Gopalan, V. Dierolf, and D. A. Scrymgeour, „Defect-domain wall interactions in trigonal ferroelectrics“, *Annu. Rev. Mater. Res.* **37**, 449 (2007).

[30] M. C. Wengler, U. Heinemeyer, E. Soergel, and K. Buse, „Ultraviolet light-assisted domain inversion in magnesium-doped lithium niobate crystals“, *J. Appl. Phys.* **98**, 064104 (2005).

[31] D. Redfield and W. J. Burke, „Optical absorption edge of $LiNbO_3$“, *J. Appl. Phys.* **45**, 4566 (1974).

[32] A. M. Mamedov, M. A. Osman, and L. C. Hajieva, „vuv reflectivity of $LiNbO_3$ and $LiTaO_3$ single crystals - application of synchrotron radiation“, *Appl. Phys. A.* **34**, 189 (1984).

[33] B. M. Jin, I. W. Kim, W. B. White, and A. S. Bhalla, „Modification of UV-VIS optical absorption properties caused by MgO incorporation in MgO-doped $LiNbO_3$ crystals“, *Mater. Lett.* **30**, 385 (1997).

[34] R. G. Smith, D. B. Fraser, R. T. Denton, and T. C. Rich, „Correlation of reduction in optically induced refractive index inhomogeneity with oh content in $LiTaO_3$ and $LiNbO_3$“, *J. Appl. Phys.* **39**, 4600 (1968).

[35] I. V. Kityk, M. Makowska-Janusik, M. D. Fontana, M. Aillerie, and F. Abdi, „Band structure treatment of the influence of nonstoichiometric defects on optical properties in $LiNbO_3$“, *J. Appl. Phys.* **90**, 5542 (2001).

[36] O. F. Schirmer, O. Thiemann, and M. Wohlecke, „Defects in $LiNbO_3$-i. experimental aspects“, *J. Phys. Chem. Solids* **52**, 185 (1991).

[37] C. C. Battle, S. Kim, V. Gopalan, K. Barkocy, M. C. Gupta, Q. X. Jia, and T. E. Mitchell, „Ferroelectric domain reversal in congruent $LiTaO_3$ crystals at elevated temperatures“, *Appl. Phys. Lett.* **76**, 2436 (2000).

[38] S. Kim, V. Gopalan, K. Kitamura, and Y. Furukawa, „Domain reversal and nonstoichiometry in lithium tantalate“, *J. Appl. Phys.* **90**, 2949 (2001).

[39] R. Mouras, M. Fontana, P. Bourson, and A. Postnikov, „Lattice site of mg ion in $LiNbO_3$ crystal determined by raman spectroscopy“, *J. Phys.: Condens. Matter* **12**, 5053 (2000).

[40] K. Kitamura, J. K. Yamamoto, N. Iyi, S. Kimura, and T. Hayashi, „Stoichiometric $LiNbO_3$ single crystal growth by double crucible Czochralski method using automatic powder supply system“, *J. Cryst. Growth* **116**, 327 (1992).

[41] P. F. Bordui, R. G. Norwood, D. H. Jundt, and M. M. Fejer, „Preparation and characterization of off-congruent lithium niobate crystals“, *J. Appl. Phys.* **71**, 875 (1992).

[42] K. Buse, „Light-induced charge transport processes in photorefractive crystals I: Models and experimental methods“, *Appl. Phys. B.* **64**, 273 (1997).

[43] K. Buse, „Light-induced charge transport processes in photorefractive crystals II: Materials“, *Appl. Phys. B.* **64**, 391 (1997).

[44] D. H. Jundt, G. Magel, M. Fejer, and R. Byer, „Periodically poled $LiNbO_3$ for high-efficiency second-harmonic generation“, *Appl. Phys. Lett.* **59**, 2657 (1991).

[45] M. M. Fejer, G. A. Magel, D. H. Jundt, and R. L. Byer, „Quasi-phase-matched second harmonic generation: Tuning and tolerances“, *IEEE J. Quantum Electron.* **28**, 2631 (1992).

[46] J. Webjorn, J. Amin, M. Hempstead, P. S. Russell, and J. S. Wilkinson, „Electric-field-induced periodic domain inversion in Nd^{3+}-diffused $LiNbO_3$“, *Electron. Lett.* **30**, 2135 (1994).

[47] A. G. Chynoweth, „Barkhausen pulses in barium titanate“, *Phys. Rev.* **110**, 1316 (1958).

[48] J. A. Armstrong, N. Bloembergen, J. Ducuing, and P. S. Pershan, „Interactions between light waves in a nonlinear dielectric“, *Phys. Rev.* **127**, 1918 (1962).

[49] V. Gopalan, T. E. Mitchell, Y. Furukawa, and K. Kitamura, „The role of nonstoichiometry in 180 degrees domain switching of $LiNbO_3$ crystals“, *Appl. Phys. Lett.* **72**, 1981 (1998).

[50] V. Bermudez, L. Huang, D. Hui, S. Field, and E. Dieguez, „Role of stoichiometric point defect in electric-field-poling lithium niobate“, *Appl. Phys. A* **70**, 591 (2000).

[51] S. Ganesamoorthy, M. Nakamura, S. Takekawa, S. Kumaragurubaran, K. Terabe, and K. Kitamura, „A comparative study on the domain switching characteristics of near stoichiometric lithium niobate and lithium tantalate single crystals“, *Mat. Sci. Eng. B* **120**, 125 (2005).

[52] W. B. Yan, Y. F. Kong, L. H. Shi, L. Sun, H. D. Liu, X. C. Li, D. Zhao, J. J. Xu, S. Chen, L. Zhang, Z. H. Huang, S. G. Liu, and G. Y. Zhang, „The relationship between the switching field and the intrinsic defects in near-stoichiometric lithium niobate crystals“, *J. Phys. D.* **39**, 21 (2006).

[53] L. Huang, D. Hui, D. J. Bamford, S. J. Field, I. Mnushkina, L. E. Myers, and J. V. Kayser, „Periodic poling of magnesium-oxide-doped stoichiometric lithium niobate grown by the top-seeded solution method“, *Appl. Phys. B.* **72**, 301 (2001).

[54] M. C. Wengler, B. Fassbender, E. Soergel, and K. Buse, „Impact of ultraviolet light on coercive field, poling dynamics and poling quality of various lithium niobate crystals from different sources“, *J. Appl. Phys.* **96**, 2816 (2004).

[55] V. Gopalan and M. C. Gupta, „Observation of internal field in $LiTaO_3$ single crystals: Its origin and time-temperature dependence“, *Appl. Phys. Lett.* **68**, 888 (1996).

[56] A. Agronin, Y. Rosenwaks, and G. Rosenman, „Direct observation of pinning centers in ferroelectrics“, *Appl. Phys. Lett.* **88**, 072911 (2006).

[57] Y. Watanabe, T. Sota, K. Suzuki, N. Iyi, K. Kitamura, and S. Kimura, „Defect structures in $LiNbO_3$“, *J. Phys.: Condens. Matter* **7**, 3627 (1995).

[58] Y. Chen, W. Yan, J. Guo, S. Chen, G. Zhang, and Z. Xia, „Effect of Mg concentration on the domain reversal of Mg-doped $LiNbO_3$“, *Appl. Phys. Lett.* **87**, 212904 (2005).

[59] G. Ravi, K. Kitamura, S. Ganesamoorthy, S. Takekawa, M. Nakamura, Y. Liu, and H. Hatano, „Growth, optical and switching characteristics of ferroelectric pure and Mn-doped near SLN crystals“, *Ferroelectrics* **332**, 51 (2006).

[60] M. Paturzo, S. Grilli, P. Ferraro, A. Finizio, P. D. Natale, N. Argiolas, M. Bazzan, M. V. Ciampolillo, and C. Sada, „Optical characterization of erbium doped $LiNbO_3$ poling properties“, *J. Appl. Phys.* **104**, 014103 (2008).

[61] V. Dierolf and C. Sandmann, „Direct-write method for domain inversion patterns in $LiNbO_3$“, *Appl. Phys. Lett.* **84**, 3987 (2004).

[62] H. Zeng, Y. Kong, H. Liu, S. Chen, Z. Huang, X. Ge, and J. Xu, „Light-induced superlow electric field for domain reversal in near-stoichiometric magnesium-doped lithium niobate“, *J. Appl. Phys.* **107**, 063514 (2010).

[63] A. Fujimura, T. Sohmura, and T. Suhara, „Fabrication of domain-inverted gratings in $MgO:LiNbO_3$ by applying voltage under ultraviolet irradiation through photomask at room temperature“, *Electron. Lett.* **39**, 719 (2003).

[64] H. Ishizuki, I. Shoji, and T. Taira, „Periodical poling characteristics of congruent MgO:LiNbO_3 crystals at elevated temperature“, *Appl. Phys. Lett.* **82**, 4062 (2003).

[65] M. Yamada and K. Kishima, „Fabrication of periodically reversed domain structure for SHG in LiNbO_3 by direct electron beam lithography at room temperature“, *Electron. Lett.* **27**, 828 (1991).

[66] J. Webjorn, V. Pruneri, P. S. Russell, J. R. M. Barr, and D. C. Hanna, „Quasi-phase-matched blue-light generation in bulk lithium-niobate, electrically poled via periodic liquid electrodes“, *Electron. Lett.* **30**, 894 (1994).

[67] K. Nakamura, J. Kurz, K. Parameswaran, and M. M. Fejer, „Periodic poling of magnesium-oxide-doped lithium niobate“, *J. Appl. Phys.* **91**, 4528 (2002).

[68] V. Gopalan and T. E. Mitchell, „Wall velocities, switching times, and the stabilization mechanism of 180 degrees domains in congruent LiTaO_3 crystals“, *J. Appl. Phys.* **83**, 941 (1998).

[69] H. A. Eggert, F. Kalkum, M. C. Wengler, U. Heinemeyer, and K. Buse, „Light-assisted generation of tailored ferroelectric domain structures“, *Ferroelectrics* **1**, 63 (2006).

[70] A. Harada and Y. Nihei, „Bulk periodically poled MgO-LiNbO_3 by corona discharge method“, *Appl. Phys. Lett.* **69**, 2629 (1996).

[71] H. Ishizuki, T. Taira, S. Kurimura, J. H. Ro, and M. Cha, „Periodic poling in 3-mm-thick MgO:LiNbO_3 crystals“, *Jpn. J. Appl. Phys.* **42**, 108 (2003).

[72] E. J. Lim, M. M. Fejer, and R. L. Byer, „2nd-harmonic generation of green light in periodically poled planar lithium niobate waveguide“, *Electron. Lett.* **25**, 174 (1989).

[73] P. W. Haycock and P. D. Townsend, „A method of poling LiNbO_3 and LiTaO_3 below T_c“, *Appl. Phys. Lett.* **48**, 698 (1986).

[74] X. Li, K. Terabe, H. Hatano, H. Zeng, and K. Kitamura, „Domain patterning thin crystalline ferroelectric film with focused ion beam for nonlinear photonic integrated circuits“, *J. Appl. Phys.* **100**, 106103 (2006).

[75] D. F. Xue, S. X. Wu, Y. C. Zhu, K. Terabe, K. Kitamura, and J. Y. Wang, „Nanoscale domain switching at crystal surfaces of lithium niobate“, *Chem. Phys. Lett.* **377**, 475 (2003).

[76] B. J. Rodriguez, R. J. Nemanich, A. Kingon, A. Gruverman, S. V. Kalinin, K. Terabe, X. Y. Liu, and K. Kitamura, „Domain growth kinetics in lithium niobate single crystals studied by piezoresponse force microscopy“, *Appl. Phys. Lett.* **86**, 012906 (2005).

[77] A. C. Muir, C. L. Sones, S. Mailis, R. W. Eason, T. Jungk, A. Hoffmann, and E. Soergel, „Direct-writing of inverted domains in lithium niobate using a continuous wave ultraviolet laser“, *Opt. Express* **16**, 2336 (2008).

[78] C. L. Sones, A. C. Muir, Y. J. Ying, S. Mailis, R. W. Eason, T. Jungk, A. Hoffmann, and E. Soergel, „Precision nanoscale domain engineering of lithium niobate via UV laser induced inhibition of poling“, *Appl. Phys. Lett.* **92**, 072905 (2008).

[79] V. Bermudez, A. Gil, L. Arizmendi, J. Colchero, A. M. Baro, and E. Dieguez, „Techniques of observation and characterization of the domain structure in periodically poled lithium niobate“, *J. Mater. Res.* **15**, 2814 (2000).

[80] E. Soergel, „Visualization of ferroelectric domains in bulk single crystals“, *Appl. Phys. B* **81**, 729 (2005).

[81] V. Gopalan and M. C. Gupta, „Origin of internal field and visualization of 180 degrees domains in congruent $LiTaO_3$ crystals“, *J. Appl. Phys.* **80**, 6099 (1996).

[82] V. Gopalan, Q. X. Jia, and T. E. Mitchell, „In situ video observation of 180 degrees domain kinetics in congruent $LiNbO_3$ crystals“, *Appl. Phys. Lett.* **75**, 2482 (1999).

[83] K. Nassau, H. J. Levinstein, and G. M. Loiacono, „Ferroelectric lithium niobate. 1. Growth, domain structure, dislocations and etching“, *J. Phys. Chem. Solids* **27**, 983 (1966).

[84] N. Nizekei, T. Yamada, and H. Toyoda, „Growth ridges etched hillocks and crystal structure of lithium niobate“, *Jpn. J. Appl. Phys.* **6**, 318 (1967).

[85] W. L. Holstein, „Etching study of ferroelectric microdomains in $LiNbO_3$ and MgO:$LiNbO_3$“, *J. Cryst. Growth* **171**, 477 (1997).

[86] C. L. Sones, S. Mailis, W. S. Brocklesby, R. W. Eason, and J. R. Owen, „Differential etch rates in z-cut $LiNbO_3$ for variable HF/HNO_3 concentrations“, *J. Mater. Chem.* **12**, 295 (2002).

[87] R. S. Cheng, W. L. Chen, and W. S. Wang, „Mach-zehnder modulators with lithium niobate ridge waveguides fabricated by proton-exchange wet etch and nickel indiffusion“, *IEEE Photonic. Tech. L.* **7**, 1282 (1995).

[88] C. E. Valdivia, *Light-induced ferroelectric domain engineering in lithium niobate & lithium tantalate*. PhD thesis, ORC, University of Southampton, 2007.

[89] D. A. Scrymgeour and V. Gopalan, „Nanoscale piezoelectric response across a single antiparallel ferroelectric domain wall“, *Phys. Rev. B* **72**, 024103 (2005).

[90] F. Johann, Y. J. Ying, T. Jungk, A. Hoffmann, C. L. Sones, R. W. Eason, S. Mailis, and E. Soergel, „Depth resolution of piezoresponse force microscopy“, *Appl. Phys. Lett.* **94**, 172904 (2009).

[91] I. W. Kim, B. C. Park, B. M. Jin, A. S. Bhalla, and J. W. Kim, „Characteristics of MgO-doped $LiNbO_3$ crystals“, *Mater Lett* **24**, 157 (1995).

[92] Y. Furukawa, K. Kitamura, S. Takekawa, K. Niwa, and H. Hatano, „Stoichiometric Mg:$LiNbO_3$ as an effective material for nonlinear optics“, *Opt. Lett.* **23**, 1892 (1998).

[93] J. Koppitz, O. F. Schirmer, and A. I. Kuznetsov, „Thermal dissociation of bipolarons in reduced undoped $LiNbO_3$“, *Europhys. Lett.* **4**, 1055 (1987).

[94] K. Nakamura, H. Ando, and H. Shimizu, „Ferroelectric domain inversion caused in $LiNbO_3$ plates by heat-treatment“, *Appl. Phys. Lett.* **50**, 1413 (1987).

[95] O. Caballero-Calero, M. Koesters, T. Woike, K. Buse, A. Garcia-Cabanes, and M. Carrascosa, „Electric field periodical poling of lithium niobate crystals after soft-proton-exchanged waveguide fabrication“, *Appl. Phys. B* **88**, 75 (Jan 2007).

[96] F. Kalkum, H. A. Eggert, T. Jungk, and K. Buse, „A stochastic model for periodic domain structuring in ferroelectric crystals“, *J. Appl. Phys.* **102**, 014104 (2007).

[97] T. Jungk, A. Hoffmann, and E. Soergel, „Contrast mechanisms for the detection of ferroelectric domains with scanning force microscopy“, *New J. Phys.* **11**, 033029 (2009).

[98] M. Lilienblum and E. Soergel, „Determination of the coercive field of ferroelectrics by piezoresponse force microscopy“, submitted (2011).

[99] X. Liu, K. Terabe, and K. Kitamura, „Stability of engineered domains in ferroelectric $LiNbO_3$ and $LiTaO_3$ crystals“, *Phys. Scr.* **T129**, 103 (2007).

[100] Y. J. Ying, *Light-assisted domain engineering, waveguide fabrication, and microstructuring of lithium niobate*. PhD thesis, ORC, University of Southampton, 2010.

[101] D. P. Birnie, „Analysis of diffusion in lithium niobate“, *J. Mater. Sci.* **28**, 302 (1993).

[102] K. Sasagawa and M. Tsuchiya, „Highly efficient third harmonic generation in a periodically poled MgO:$LiNbO_3$ disk resonator“, *Appl. Phys. Express* **2**, 122401 (Jan 2009).

[103] T. Beckmann, H. Linnenbank, H. Steigerwald, B. Sturman, D. Haertle, K. Buse, and I. Breunig, „Highly tunable low-threshold optical parametric oscillation in radially poled whispering gallery resonators“, *Phys. Rev. Lett.* accepted (2011).

[104] B. E. Little, J. P. Laine, and H. A. Haus, „Analytic theory of coupling from tapered fibers and half-blocks into microsphere resonators“, *J. Lightwave Technol.* **17**, 704 (1999).

[105] K. Mizuuchi, A. Morikawa, T. Sugita, and K. Yamamoto, „Electric-field poling in Mg-doped $LiNbO_3$“, *J. Appl. Phys.* **96**, 6585 (2004).

[106] H. Steigerwald, F. Luedtke, and K. Buse, „Ultraviolet light assisted periodic poling of near-stoichiometric, magnesium-doped lithium niobate crystals“, *Appl. Phys. Lett.* **94**, 032906 (2009).

[107] A. Kuroda, S. Kurimura, and Y. Uesu, „Domain inversion in ferroelectric MgO:$LiNbO_3$ by applying electric fields“, *Appl. Phys. Lett.* **69**, 1565 (1996).

[108] V. Y. Shur, E. L. Rumyantsev, R. G. Batchko, G. D. Miller, M. M. Fejer, and R. L. Byer, „Domain kinetics in the formation of a periodic domain structure in lithium niobate“, *Phys. Solid State+* **41**, 1681 (1999).

[109] K. Buse, S. Breer, K. Peithmann, S. Kapphan, M. Gao, and E. Krätzig, „Origin of thermal fixing in photorefractive lithium niobate crystals“, *Phys. Rev. B* **56**, 1225 (1997).

[110] H. Steigerwald, M. Lilienblum, F. von Cube, Y. J. Ying, R. W. Eason, S. Mailis, B. Sturman, E. Soergel, and K. Buse, „Origin of UV-induced poling inhibition in lithium niobate crystals“, *Phys. Rev. B* **82**, 214105 (2010).

[111] B. Briat, V. G. Grachev, G. I. Malovichko, O. F. Schirmer, and M. Woehlecke *Photorefractive Materials and Their Applications* 2. Springer, New York, 2007.

[112] A. C. Muir, G. J. Daniell, C. P. Please, I. T. Wellington, S. Mailis, and R. W. Eason, „Modelling the formation of optical waveguides produced in $LiNbO_3$ by laser induced thermal diffusion of lithium ions“, *Appl. Phys. A* **83**, 389 (2006).

[113] A. Einstein and M. von Smoluchowski *Untersuchungen über die Theorie der Brownschen Bewegung*. Verlag Harri Deutsch, Frankfurt a. M., 2001.

[114] A. Mehta, E. K. Chang, and D. M. Smyth, „Ionic transport in $LiNbO_3$“, *J Mater Res* **6**, 851 (1991).

[115] B. I. Sturman, M. Carrascosa, F. Agulló-López, and J. Limeres, „Theory of high-temperature photorefractive phenomena in $LiNbO_3$ crystals and applications to experiment“, *Phys. Rev. B* **57**, 12792 (1998).

[116] L. D. Landau and E. M. Lifshits *The electrodynamics of continuous media*. Pergamon Press, Oxford, 1984.

[117] L. A. Girifalco *Statistical Mechanics of Solids*. Oxford University Press, New York, 2003.

[118] V. E. Wood, N. F. Hartman, A. E. Austin, and C. M. Verber, „stoichiometry dependence of lithium out-diffusion in $LiNbO_3$“, *J. Appl. Phys.* **52**, 1118–1120 (1981).

[119] S. Mailis, C. Riziotis, I. T. Wellington, P. G. R. Smith, C. B. E. Gawith, and R. W. Eason, „Direct ultraviolet writing of channel waveguides in congruent lithium niobate single crystals“, *Opt. Lett.* **28**, 1433 (2003).

[120] P. Ganguly, C. L. Sones, Y. J. Ying, H. Steigerwald, K. Buse, E. Soergel, R. W. Eason, and S. Mailis, „Determination of refractive indices from the mode profiles of UV-written channel waveguides in $LiNbO_3$-crystals for optimization of writing conditions“, *J. Lightwave Technol.* **27**, 3490 (2009).

[121] Y. N. Korkishko and V. Vederov, „Structural phase diagram of $H_xLi_{1-x}NbO_3$ waveguides: The correlation between optical and structural properties“, *IEEE J. Sel. Top. Quant* (1996).

[122] K. Mizuuchi, A. Morikawa, T. Sugita, and K. Yamamoto, „Polarisation-switching-induced resistance change in ferroelectric mg-doped $LiNbO_3$ single crystals“, *Electron. Lett.* **40**, 819 (2004).

[123] T. Jungk and E. Soergel, „Depth-resolved analysis of ferroelectric domain structures in bulk $LiNbO_3$ crystals by scanning force microscopy“, *Appl. Phys. Lett.* **86**, 242901 (2005).

[124] M. Tasson, H. Legal, J. C. Peuzin, and F. C. Lissalde, „Orientation mechanisms of spontaneous polarization in lithium niobate close to curie point“, *Phys. Stat. Sol. A* **31**, 729 (1975).

[125] Y. S. Luh, R. S. Feigelson, M. M. Fejer, and R. L. Byer, „Ferroelectric domain structures in $LiNbO_3$ single-crystal fibers“, *J. Cryst. Growth* **78**, 135 (1986).

[126] H. Steigerwald, Y. J. Ying, R. E. Eason, K. Buse, S. Mailis, and E. Soergel, „Direct writing of ferroelectric domains on the x- and y-faces of lithium niobate using a continuous wave ultraviolet laser“, *Appl. Phys. Lett.* **98**, 062902 (2011).

[127] L. Gui, H. Hu, M. Garcia-Granda, and W. Sohler, „Local periodic poling of ridges and ridge waveguides on x- and y-cut $LiNbO_3$ and its application for second harmonic generation“, *Opt Express* **17**, 3923 (2009).

[128] Y. H. Chen, J. H. Yao, B. X. Yan, H. L. Deng, Y. F. Kong, S. L. Chen, J. J. Xu, and G. Y. Zhang, „Harmonic violet light generation in periodically poled bulk near-stoichiometric MgO-doped $LiNbO_3$“, *Opt. Comn.* **224**, 149 (2003).

[129] H. Xu, D. Lee, S. B. Sinnott, V. Dierolf, V. Gopalan, and S. R. Phillpot, „Structure and diffusion of intrinsic defect complexes in $LiNbO_3$ from density functional theory calculations“, *J. Phys-Condens. Mat.* **22**, 135002 (2010).

[130] V. Gopalan and M. C. Gupta, „Origin and characteristics of internal fields in $LiNbO_3$ crystals“, *Ferroelectrics* **198**, 49 (1997).

[131] J. H. Yao, Y. H. Chen, B. X. Yan, H. L. Deng, Y. F. Kong, S. Chen, J. J. Xu, and G. Y. Zhang, „Characteristics of domain inversion in magnesium-oxide-doped lithium niobate“, *Physica B* **352**, 294 (2004).

[132] A. Savage, „Pyroelectricity and spontaneous polarization in $LiNbO_3$“, *J. Appl. Phys.* **37**, 3071 (1966).

[133] H. Steigerwald, F. von Cube, F. Luedtke, V. Dierolf, and K. Buse, „Influence of heat and UV light on the coercive field of lithium niobate crystals“, *Appl. Phys. B* **101**, 535 (2010).

[134] F. Jermann, M. Simon, and E. Krätzig, „Photorefractive properties of congruent and stoichiometric lithium niobate at high light intensities“, *J. Opt. Soc. Am. B* **12**, 2066 (1995).

[135] Y. Furukawa, K. Kitamura, Y. Ji, G. Montemezzani, M. Zgonik, C. Medrano, and P. Gunter, „Photorefractive properties of iron-doped stoichiometric lithium niobate“, *Opt. Lett.* **22**, 501 (1997).

[136] I. E. Barry, G. W. Ross, P. G. R. Smith, R. W. Eason, and G. Cook, „Microstructuring of lithium niobate using differential etch-rate between inverted and non-inverted ferroelectric domains“, *Mater. Lett.* **37**, 246 (1998).

Chapter 6

Summary

Lithium niobate has become the material of first choice for nonlinear optical applications in the visible and near-infrared. Even nowadays, however, it remains challenging to fabricate ferroelectric domain patterns at a length scale of sub-to-few microns that meet the requirements of their potential applications in $LiNbO_3$ for non-linear optics. The understanding of fundamental properties of domain growth and the development of methods for domain engineering are both closely related and both treated in this thesis.

In the context of this work, the influence of external parameters like temperature and UV light intensity as well as intrinsic parameters like stoichiometry and doping on the poling behavior of lithium niobate crystals have been investigated. Underlying mechanisms for coercive field reduction in $LiNbO_3$ have been identified as reorientation of frustrated defect clusters for heating and screening of defects by photo-excited electrons for illumination with weakly absorbed UV light.

For the case of elevated temperatures, at temperatures as low as 500 K, lithium ions inside the crystal have sufficient mobility that defect clusters with their dipole moment oriented antiparallel to the spontaneous polarization can be re-oriented. This leads to less domain wall pinning and therefore lowers the field that is needed to invert the spontaneous polarization. In the case of illumination with weakly absorbed UV light ($\lambda = 334$ nm and $\lambda = 351$ nm) of Mg-doped material, the photo-conductivity is significantly increased, which efficiently screens defect structures, so domain wall pinning is reduced and the coercive field is lowered.

UV illumination and elevated temperatures can be superimposed leading to an overall reduction of the coercive field strength of Mg-doped congruent $LiNbO_3$ to 1 kV/mm. Structured illumination by weakly absorbed UV light is utilized for domain patterning in lithium niobate crystals and

Acknowledgements

I would like to thank Prof. Dr. Karsten Buse for welcoming me to his group as a PhD student and for his support throughout my thesis. I appreciate the good working environment provided by him.

Thanks to Prof. Dr. Karl Maier for conducting the review of my thesis and for the friendly collaborations with his group. Thanks also to Prof. Dr. Rob Eason and Prof. Dr. Moritz Sokolowski for the secondary reviews.

Special thanks to PD Dr. Elisabeth Soergel and her PFM-team for a good collaboration and especially to Elisabeth for unvarnished feedback during scientific discussions that improved the quality of this thesis. I had the opportunity to collaborate with other research groups and I am grateful for that. Just to mention a few, I would like to thank Dr. Sak Mailis and Dr. Charlie Ying from ORC Southampton, who were partners in a vivid collaboration, Prof. Dr. Volkmar Dierolf and his team who welcomed me at Lehigh University for a research internship and of course Dr. Lena Jentjens and Dr. Konrad Peithmann from the HISKP of the University of Bonn, who were always open for discussions and sharing recourses. Also thanks to Prof. Dr. Boris Sturman for many scientific discussions.

During my thesis, I was in the lucky position to work with three excellent diploma students: Fabian Lüdtke, Niklas Waasem and Felix von Cube contributed tremendously to the scientific work presented in this thesis and each one of them is an awesome guy.

Thanks also to Ms. Raja Bernard for taking care of all administrative issues and Dr. Akos Hoffmann for his technical assistance. I would like to thank all current and former members of the Hertz team, who supported me.

I am aware that without the support of my friends and my family I would not have succeeded and I am truly grateful for this. Especially Marc, Tine and Donna but also many other dear friends, each in their own way, have been contributing to my work-life balance for many years. My sisters Annette and Kathrin and my parents ever since have been a great support in my life and I owe them a lot.

List of publications

- H. Steigerwald, Y. J. Ying, R. W. Eason, K. Buse, S. Mailis, and E. Soergel, "Direct writing of ferroelectric domains on the x- and y-faces of lithium niobate using a continuous wave ultraviolet laser," Appl. Phys. Lett. **98**, 062902 (2011).
- H. Steigerwald, M. Lilienblum, F. von Cube, Y. J. Ying, R. W. Eason, S. Mailis, B. Sturman, E. Soergel, and K. Buse, "Origin of UV-induced poling inhibition in lithium niobate crystals," Phys. Rev. B **82**, 214105 (2010).
- H. Steigerwald, F. von Cube, F. Luedtke, V. Dierolf, and K. Buse, "Influence of heat and UV light on the coercive field of lithium niobate crystals," Appl. Phys. B **101**, 535 (2010).
- L. Jentjens, K. Peithmann, K. Maier, H. Steigerwald, T. Jungk, "Radiation-damage-assisted ferroelectric domain structuring in magnesium-doped lithium niobate," Appl. Phys. B **95**, 441 (2009).
- F. Luedtke, J. Villarroel, A. García-Cabañes, M. Carrascosa, H. Steigerwald, K. Buse "Mach-Zehnder method for optical damage characterization of planar waveguides," Ferroelectrics **390**, 41 (2009).
- P. Ganguly, C. L. Sones, Y. J. Ying, H. Steigerwald, K. Buse, E. Soergel, R. W. Eason, and S. Mailis, "Determination of refractive indices from the mode profiles of UV-written channel waveguides in $LiNbO_3$-crystals for optimization of writing conditions," J. Lightwave Technol. **27**, 3490 (2009).
- H. Steigerwald, F. Luedtke, and K. Buse, "Ultraviolet light assisted periodic poling of near-stoichiometric, magnesium-doped lithium niobate crystals," Appl. Phys. Lett. **94**, 032906 (2009).